



Simulation studies of a 30-keV MR-ToF device for highly sensitive collinear laser spectroscopy

F.M. Maier^{a,b,*}, M. Vilen^a, I. Belosevic^c, F. Buchinger^d, C. Kanitz^{a,e}, S. Lechner^{a,d}, E. Leistenschneider^a, W. Nörtershäuser^f, P. Plattner^{a,g}, L. Schweikhard^b, S. Sels^a, F. Wienholtz^{a,f}, S. Malbrunot-Ettenauer^a

^a Experimental Physics Department, CERN, CH-1211, Geneva 23, Switzerland

^b Institut für Physik, Universität Greifswald, 17487 Greifswald, Germany

^c TRIUMF, 4004 Wesbrook Mall, Vancouver, BC V6T 2A3, Canada

^d McGill University, Montréal, Québec, H3A 2T8, Canada

^e Department für Physik, Friedrich-Alexander-Universität Erlangen-Nürnberg, 91058 Erlangen, Germany

^f Institut für Kernphysik, Technische Universität Darmstadt, Schlossgartenstr. 9, 64289 Darmstadt, Germany

^g Universität Innsbruck, Innrain 52, 6020 Innsbruck, Austria

ARTICLE INFO

Keywords:

Collinear laser spectroscopy
MR-ToF device
Short-lived radionuclides
MIRACLS
SimIon simulations
Ion trapping

ABSTRACT

The Multi Ion Reflection Apparatus for Collinear Laser Spectroscopy (MIRACLS) seeks to extend the reach of high-resolution collinear laser spectroscopy (CLS) to more exotic radionuclides. In this novel technique, ion bunches of short-lived radioisotopes are trapped between two electrostatic mirrors of a Multi-Reflection Time-of-Flight (MR-ToF) device at 30-keV kinetic energy. The same ion bunch can be probed by a spectroscopy laser for thousands of times compared to a single probing in the traditional CLS measurement scheme. Thus, the experimental sensitivity is increased by more than one to two orders of magnitude. Extensive simulations are presented, demonstrating the feasibility of high-resolution collinear laser spectroscopy (CLS) in the newly envisioned MR-ToF apparatus operating at ion energies of 30 keV. Once the mechanical design and operational parameters are optimized for the requirements of CLS, the spectral line is neither significantly broadened nor distorted by the combination of CLS and MR-ToF operation. According to the simulations, the storage efficiency and the ion-laser overlap are suitable for laser excitation of the majority of the trapped ions. In summary, > 90% injection and storage efficiency, > 75% ion-laser overlap and a line width approaching the natural line width of the transition of interest are reached in the simulation.

1. Introduction

For more than four decades fluorescence-based Collinear Laser Spectroscopy (CLS) has been employed to determine ground-state properties of short-lived radionuclides [1–5]. In this technique, a beam of ionic or neutral atoms is superimposed with a continuous-wave, narrow-band laser beam. Fluorescence photons from excited ionic or neutralized atoms are detected by photomultiplier tubes. By scanning the laser around the resonance frequency, the hyperfine structure of the optical transition is obtained. To increase the signal-to-noise ratio, current state-of-the-art CLS experiments employ bunched ion beams formed in a Paul trap cooler-buncher [2,6]. Due to its high precision, accuracy and resolution, CLS is a powerful experimental technique for accessing nuclear spins, electromagnetic moments and mean square charge radii of short-lived radionuclides and hence provides insight into the nuclear structure far away from stability.

However, conventional fluorescence-based CLS is limited to nuclides with production yields of typically more than several thousands or even ten-thousands ions per second [5]. Hence, there is a strong demand to extend the reach of high-resolution laser spectroscopy to the most exotic radionuclides with very low production yields as available at radioactive ion beam facilities. To this end, innovative methods such as Collinear Resonance Ionization Spectroscopy (CRIS) [7–9], high-resolution in-source laser spectroscopy [10], in-gas jet spectroscopy [11,12], laser cooling of radioactive ions [13] or more specialized techniques [14] have been or are being developed. Most recently, the novel Multi Ion Reflection Apparatus for CLS (MIRACLS), currently under construction at ISOLDE/CERN, has been envisioned to improve the experimental sensitivity of fluorescence-based CLS itself [15–19]. In this setup, 30-keV ion bunches will be trapped between two electrostatic mirrors of a multi-reflection time-of-flight (MR-ToF)

* Corresponding author at: Experimental Physics Department, CERN, CH-1211, Geneva 23, Switzerland.

E-mail address: franziska.maria.maier@cern.ch (F.M. Maier).

device, allowing the laser beam to probe the ions during each revolution. Thus, the observation time will be extended and the experimental sensitivity will be increased by more than one to two orders of magnitude [20]. The actual improvement depends on the half-life and mass of the nuclide, the ionic transition and the achievable trapping time in the MR-ToF device without significant beam losses through collisions with residual gas or loss of the bunched-beam structure.

Over the years, MR-ToF instruments have become indispensable tools for precision mass measurements and mass separation of short-lived radionuclides at radioactive ion beam facilities throughout the world, see e.g. [21–30]. As a novel application of MR-ToF devices, the MIRACLS project aims to extend the reach of fluorescence-based collinear laser spectroscopy techniques.

As first science cases for MIRACLS, neutron-rich Magnesium (Mg) isotopes in the $N = 20$ island of inversion [31] and Cadmium (Cd) isotopes at and beyond the $N=50$ and $N=82$ neutron shell closures will be studied, extending previous measurements with traditional CLS [32,33]. Nuclear charge radii obtained in these measurements will serve as important benchmarks for modern nuclear theory, such as the Fayans-based nuclear density functional theory [32,34–37] or leading ab-initio methods, which have made remarkable progress over the last decade [34,35,37,38] and are now capable to predict electromagnetic ground state properties of exotic radionuclides even in mid-shell regions [39–41].

In both, Mg and Cd, even–even isotopes form a closed two-level system in their ionic structure in which laser-excited ions decay back to the ionic ground state. As a consequence, they can in principle be probed indefinitely by a laser beam. Hence, without any pumping to other (hyper)fine structure states, these isotopes are ideal first science cases with maximal sensitivity for the novel MIRACLS approach. Additionally, development work is ongoing to extend the MIRACLS technique beyond closed-two level systems [42]. For instance, an additional (broad-band) laser beam can be utilized to depopulate a dark, metastable (fine-structure) state or to redistribute the population among the available hyperfine states.

In previous studies, a MIRACLS proof-of-principle experimental campaign was successfully performed to demonstrate the potential of CLS within a 1.5-keV MR-ToF device [15–20]. Additionally, its results have established the validity of ion-optical simulation tools for CLS in this setup [15,20]. Hence, the same simulation approach is applied to design a high-resolution MIRACLS. In order to obtain a spectral resolution that approaches the natural line width in conventional CLS, fast ion beams with a kinetic energy E of tens of keV are employed. This minimizes the Doppler broadening σ_f of the measured transition frequency according to $\sigma_f \propto \sigma_E/\sqrt{E}$ [43], where σ_E is the energy spread of the ions. However, MR-ToF devices built so far utilize ion beam kinetic energies around a few keV and mirror potentials of less than 8 kV [21–30,44–47]. Therefore, a MR-ToF device capable of trapping ions with 30-keV kinetic energy is envisioned for a high-resolution MIRACLS.

In the present work, extensive simulation studies of this new device and its injection optics are performed to guide physical design and initial operation of the setup. Different geometries and combinations of the electric potentials for the injection optics as well as MR-ToF mirrors are explored. The design with the best performance achieved that simultaneously meets the space requirements of the experimental hall at ISOLDE/CERN is discussed in more detail. Special emphasis is given to the parameters relevant for CLS at MIRACLS. These are the ion-storage efficiency, the ion–laser overlap and the Doppler broadening governed by the energy spread as well as the angular spread of the ions' motion with respect to the laser beam axis. Moreover, several sources of systematic effects are investigated in this manuscript. The simulation results for CLS in the envisioned 30-keV MR-ToF apparatus show the conceptual feasibility and potential of high-resolution CLS in an MR-ToF device. This offers a strong foundation for realizing the planned apparatus.

2. Experimental setup

A schematic overview of the MIRACLS setup currently being under construction at ISOLDE/CERN is presented in Fig. 1. After formation of the radioactive ion beam at the ISOLDE target station, electrostatic acceleration and mass selection by a magnetic mass separator, the ions are injected into MIRACLS' linear buffer-gas-filled Paul trap for cooling and bunching of the ion beam [48,49]. The Paul trap is floated to 50 kV. Following the extraction of the ions from the Paul trap as ion bunches, the ions are accelerated to a kinetic energy of 2 keV, i.e. the beamline beyond the Paul trap is floated to 48 kV, accordingly. Afterwards the ion beam is focused by three electrostatic einzel lenses (L1–L3) enabling parallel-to-parallel focusing and bent by a 30-degree deflector to overlap it with the laser beam. Subsequently, the ions pass through two more einzel lenses (L4 and L5) and are reaccelerated to 50 keV shortly before they reach the MR-ToF device. Lens L5 differs from the other einzel lenses L1–L4 by its much larger focusing capability given its higher field strength. The reacceleration region consisting of a conical electrode is modelled after Refs. [50,51]. The 2-keV section of the transfer beamline is floated to 48 kV, see above, while the vacuum chambers around the MR-ToF device remain on ground potential. Hence a HV break is installed between the high-voltage lens L5 and the reacceleration cone, which is shielded by an inner cylinder to which a potential of 48 kV is applied.

After reacceleration to 50 keV, the ions are captured at 30-keV beam energy in an MR-ToF device via the technique of in-trap lift switching [52]. A 20-kV potential difference has been chosen such that the ions will easily overcome the maximum in the electric potentials applied to the mirror electrodes (around 40 kV) when the ions are injected into the MR-ToF device (see Section 3). Mirror switching is a technical challenge for a 30-keV MR-ToF device due to the high potentials needed at the individual mirror electrodes. This motivates the choice of the in-trap lift for the ion capture and extraction.

The MR-ToF device (see also Section 3) consists of two opposing electrostatic mirrors with a central drift tube in between (electrode 7, see Fig. 2(top)). Each electrostatic mirror consists of six electrodes (1–6). The two mirror electrodes (1–2) that are closest to the central drift tube provide radial refocusing of the ion cloud. The axial trapping potential is realized by the four outermost mirror electrodes (3–6). Between the central drift tube and the mirror electrodes two additional electrodes (8–9) are installed, which can be used as electrodes for ion monitoring and diagnostics by pickup of image-charge signals [53] or, if azimuthally segmented, as deflector electrodes [54]. The inner diameter of electrodes 7–9 is reduced to 40 mm compared to the inner diameter of the mirror electrodes of 80 mm in order to maximize the size of the field-free region in the central drift tube. Given the sensitivity of the ions' trajectories to field distortions at the point where the ions are reflected, the so-called turn-around point, the outermost mirror electrode 6 is reduced at its outer end to an inner diameter of 40 mm to shield the MR-ToF region from external electric fields. Grounded electrodes (0) in front and behind the MR-ToF device provide an additional shielding from fringe fields [20]. The planned beamline geometry provides spaces for ion diagnostics along the ions' path, including a retractable ion detector downstream of the MR-ToF device.

3. The 30-keV MR-ToF device: design and simulations¹

To find suitable MR-ToF geometries and potentials applied to individual electrodes, trajectories of the ions are simulated using the ion-optical software package SimIon, version 8.1 [55]. Firstly, the geometry of all electrodes is defined in a three dimensional grid with constant node spacing. On every grid point, the Laplace equation is solved numerically to obtain the electric potential. After definition of

¹ This section and the last paragraph of the previous section are partly reproduced from chapter 5 of the MSc thesis of F.M. Maier, see [20].

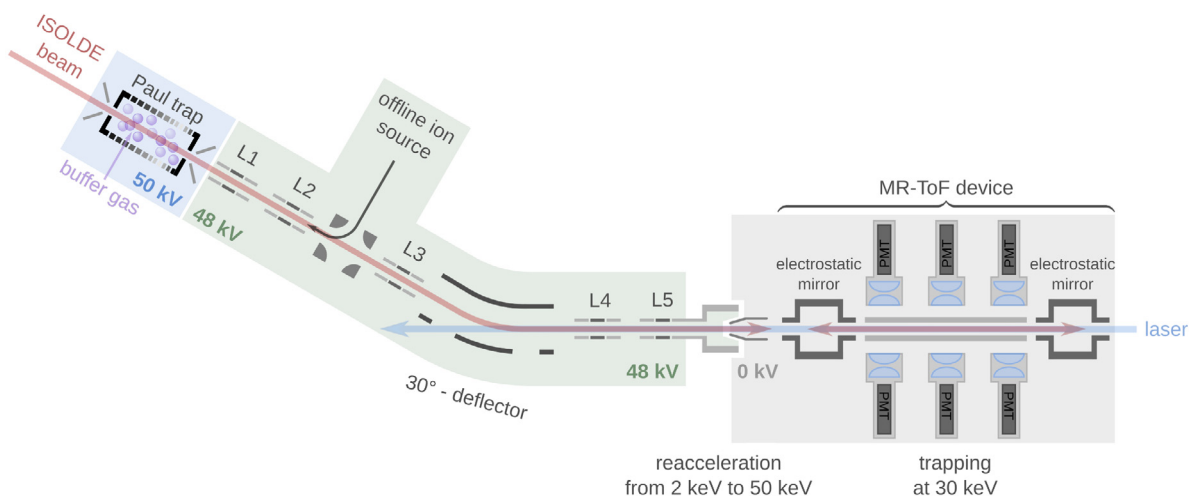


Fig. 1. Schematic overview of the MIRACLs setup for high-resolution laser spectroscopy at ISOLDE, which takes up a floor space of around $1.5 \text{ m} \times 4.4 \text{ m}$. After ion preparation of the incoming ISOLDE beam in a Paul trap, ion bunches are transported to the MR-ToF device via a $\approx 1.9\text{-m}$ long transfer beamline consisting of totally 5 einzel lenses and a 30-degree deflector. The Paul trap section is floated to 50 kV (blue shaded region, the 2-keV section of the transfer beamline is floated to 48 kV (green shaded region) and the beamline around the MR-ToF device is on ground potential (grey shaded region). A quadrupole bender installed between the einzel lenses L2 and L3 facilitates injection of stable ions from an offline ion source for testing and calibration of the MR-ToF components and the ion–laser interaction. The optical detection region consisting of six photo multiplier tubes (PMTs) is located between the two electrostatic mirrors of the MR-ToF device. The figure is not to scale. See text for details.

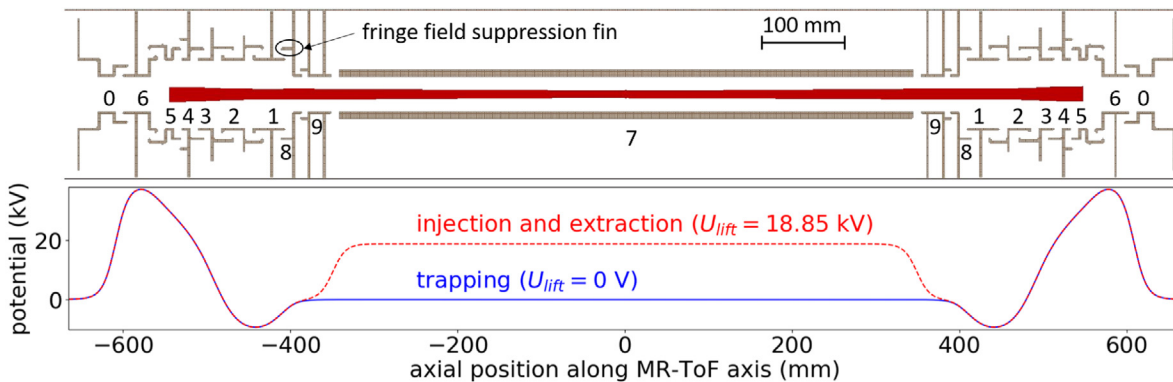


Fig. 2. MIRACLs 30-keV MR-ToF device: (Top) Cut view of its electrode structure together with the ions' simulated trajectories (in red) for 300 ions performing 300 revolutions. (Bottom) Electric potential along the central axis of the MR-ToF device once for trapping (blue) and once for injection and extraction (red) with an in-trap lift potential of $U_{\text{lift}} = 18.85 \text{ kV}$.

the ions' initial conditions such as the ion mass, position and energy, the ion trajectories are calculated for every time step in the previously calculated fields. It is possible to modify certain aspects of the simulation during the ions' flight via user programming in Lua, e.g. to include buffer-gas collisions [56] or time-dependent fields. The resulting ion parameters such as velocity or position can be recorded at user-defined planes. Coulomb interactions between ions and between ions and image charges on the electrodes are not taken into account in the simulations discussed in the present work. These so-called space-charge effects are neglected since due to the low yields only up to a few 100 ions will be stored simultaneously in the 30-keV MR-ToF device in CLS mode. For the neutron-rich Mg isotopes isobaric contamination is not expected to be present in notable amounts in the ion beam. In case of sizeable amounts of contamination, MIRACLs can take advantage of the MR-ToF's capability for mass separation. For example, the deflector electrodes between the central drift tube and the mirror electrodes will allow to remove unwanted contaminants, see e.g. [54]. Further details of the simulation procedure and investigations of the accuracy achieved can be found in the [Appendix](#).

The simulation is started with $^{24}\text{Mg}^+$ ions positioned at the middle plane of the MR-ToF device, i.e. the plane at the centre of the drift tube perpendicular to the axis. The ion beam has a transversal rms emittance of $3 \pi \text{ mm mrad}$. The kinetic energy is Gaussian distributed

around a centre of 30 keV with a standard deviation of 0.4 eV. Note that the simulations of the MIRACLs Paul trap predict a standard deviation of the energy of around 0.4 eV and a transversal rms emittance of $< 1 \pi \text{ mm mrad}$ [48]. Existing Paul traps (e.g. [57–59]) such as ISCOOL at ISOLDE show a transversal rms emittance of around $2 \pi \text{ mm mrad}$ [60]. Hence the chosen rms emittance of $3 \pi \text{ mm mrad}$ depicts a worse case scenario in the simulations.

The potentials of the six mirror electrodes are optimized in a Monte-Carlo manner similarly as performed in Ref. [15]. Due to the risk of electric discharges across the mirror electrodes, we limit our choice to potential sets in which the difference in electric potentials between neighbouring electrodes is less than 40 kV. To reduce the size of the parameter space of the potential of the two innermost mirror electrodes (1–2) are chosen to be identical. At a later stage, different potentials can be applied to these two electrodes to allow some fine tuning in the experiment. The properties of the ions are recorded whenever they pass the middle plane of the MR-ToF device in collinear direction. Storage efficiency, ion–laser overlap, Doppler broadening and increase of ion-bunch width as a function of revolution number are determined. The storage efficiency is calculated as the fraction of ions that remain trapped after 100 revolutions. The ion–laser overlap is computed as an average over all 300 simulated revolutions of the fraction of ions with a transversal displacement from the MR-ToF axis

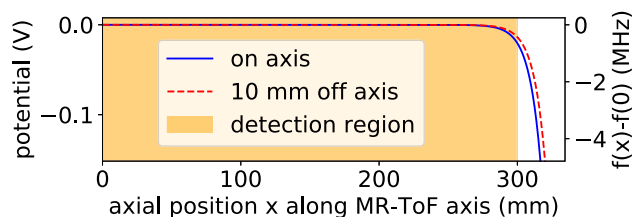


Fig. 3. Electric potential and the change of the Doppler-shifted frequency $f(x) - f(0)$ (D2 line in Mg^+ ions) for a kinetic energy of 30 keV, once for a $^{24}\text{Mg}^+$ ion flying along the central axis and once on a parallel line shifted 10 mm off axis. The length of the optical detection region is marked in orange. The central drift tube itself is extending from -345 to 345 mm.

smaller than the assumed laser beam radius of either 2 mm or 4 mm at the middle plane. For simplicity it is assumed that the laser beam is homogeneous within the assumed radius. The Doppler broadening is given by the FWHM of the Doppler-shifted resonance frequencies f calculated in the laboratory frame,

$$f = f_0 \frac{\sqrt{1 - \left(\frac{v}{c}\right)^2}}{1 - \frac{v \cos \alpha}{c}}, \quad (1)$$

where f_0 is the resonance frequency in the rest frame of the ions, c is the speed of light, v the velocity of individual ions and α is the angle between an individual ion path and the laser beam axis. The latter is assumed to be identical to the central axis of the MR-ToF device.

The Monte-Carlo optimization of the potentials applied to the individual electrodes is repeated for different geometries of the MR-ToF device, which are all guided by the design of the Greifswald MR-ToF device operating at 1.3 keV [54,61]. The lengths of the six mirror electrodes are kept fixed to the values of the Greifswald MR-ToF device while the inner electrode diameters are enlarged by a factor 2.7 for better field conformity in radial direction and hence reduced aberrations [62]. Fringe-field suppression fins are added to the individual mirror electrodes to prevent any fringe fields from outside reaching into the MR-ToF device, see Fig. 2 (top). The simulations show that the existence and design of the fringe field suppression fins as well as the gap dimensions between the individual electrodes have minimal to no effect on ion–laser overlap or Doppler broadening whereas they can significantly alter the evolution of an ion-bunch’s temporal width over revolution number. After modifying the gap size and redesigning the fringe field suppression fins the bunched-beam structure is preserved for almost a factor 3 higher revolution number. This is beneficial for the boost in sensitivity at MIRACLS to suppress background, see Section 5.3.

Only in a field-free region the ion velocity is fully independent of an ion’s position in the central drift tube. In practice, remaining potential gradients result in slightly different velocities and hence different Doppler-shifted laser frequencies in the rest frame of the ion. Hence, the length of the central drift tube (electrode 7 in Fig. 2) is chosen to be 690 mm, such that the change in electric potential along the MR-ToF axis is less than 0.1 V within a region with a length of 62 cm (see Fig. 3). For the $3s^2S_{1/2} \rightarrow 3p^2P_{3/2}$ (D2) transition in $^{24}\text{Mg}^+$ ions, for instance, a 0.1-V potential change corresponds to a change of the Doppler-shifted frequency of less than 3 MHz for an ion with 30-keV kinetic energy. In the case of the $5s^2S_{1/2} \rightarrow 5p^2P_{3/2}$ (D2) transition in the Cd^+ ions a 0.1 V change corresponds to less than 2 MHz change. This is significantly smaller than the systematic uncertainties of traditional single-passage CLS, see for instance Ref. [33] for measurements of exotic Mg isotopes. Given the lifetime of around 3.8 ns of the excited state in the D1 and D2 transitions for the Mg^+ ions [63] and the kinetic energy in the MR-ToF device, an excited ion will typically travel less than 2 mm until it decays back to the ground state. For the selected transition in Cd^+ , the lifetime of the excited state is around 2.6 ns [64],

Table 1

Potentials for the MR-ToF mirror electrodes as obtained in the Monte-Carlo approach for $^{24}\text{Mg}^+$ ions with 30-keV beam energy. See text and Fig. 2.

Respective electrode	Potential (V)
1 (innermost mirror)	-12,469.3
2	-12,469.3
3	23,002.6
4	25,966.4
5	29,648.9
6 (outermost mirror)	39,013.0

hence the travelling distance is even smaller. Thus photons emitted by ions excited outside the optical detection region at different velocities (and therefore other resonance frequencies in the laboratory frame) will not be detected.

A suitable MR-ToF geometry leading to high storage efficiency, high ion–laser overlap, small Doppler broadening and a small increase of temporal bunch width over revolution number is presented in Fig. 2 (top). The resulting potential distribution along the MR-ToF axis is shown in Fig. 2 (bottom) and the individual electrostatic potentials are listed in Table 1.

4. Simulations of the injection beamline

In the second step of the simulations, suitable injection optics for the 30-keV MR-ToF device is obtained. To start with a realistic initial ion distribution in phase space, simulations of the ion preparation in a dedicated MIRACLS Paul trap cooler-buncher [48] are performed. Ions are positioned at the potential minimum of the Paul trap and left to thermalize with room-temperature buffer gas. The buffer-gas cooling is modelled with SimIon’s built-in hard-sphere interaction model [56]. For a similar Paul trap at the MIRACLS proof-of-principle apparatus, the buffer-gas cooling simulations show an excellent agreement with experimental data [13,15]. After extraction of the ion bunches from the Paul trap, they pass the ion optical elements as described in Section 2. Subsequently, they are trapped in the MR-ToF device via the in-trap lift switching technique [52].

The potentials applied to ion-optical elements along the transport beamline from the Paul trap to the MR-ToF device are optimized via SimIon’s built-in Nelder–Mead algorithm [65]. The MR-ToF mirror potentials are kept fixed to the values obtained in Section 3. The objective function of the optimization has been tailored for minimal ion losses in the transport beamline and for a maximal storage efficiency in the MR-ToF device, simultaneously. Once good settings are found for these, the individual potentials of the transport beamline elements are varied in the next optimization step around their previous values to additionally obtain a high ion–laser overlap and a small Doppler broadening while maintaining the best storage efficiency as obtained before.

In principle, a small radial ion-beam size is desired in CLS which allows for an optimal ion–laser overlap with reduced laser diameters and, thus, little laser stray light and higher power densities. At the same time, one aims for ion trajectories which are as parallel as possible to minimize the contribution of diverging ion-beam propagation to the Doppler broadening. In practice, however, the ion bunch’s angular divergence and transversal spatial width are related to each other through the conserved transversal emittance. The latter is governed by the beam preparation in the Paul trap. The repeated reflections in the MR-ToF device couple the ion’s radial displacement and the angles of their trajectories. Thus, when observed over many revolutions in the MR-ToF instrument, one generally obtains a suboptimal laser–ion overlap, an increased Doppler broadening or both. As a consequence, many combinations of injection beamline potentials lead to a large storage efficiency, but only a few of them also result in a good performance for CLS operation.

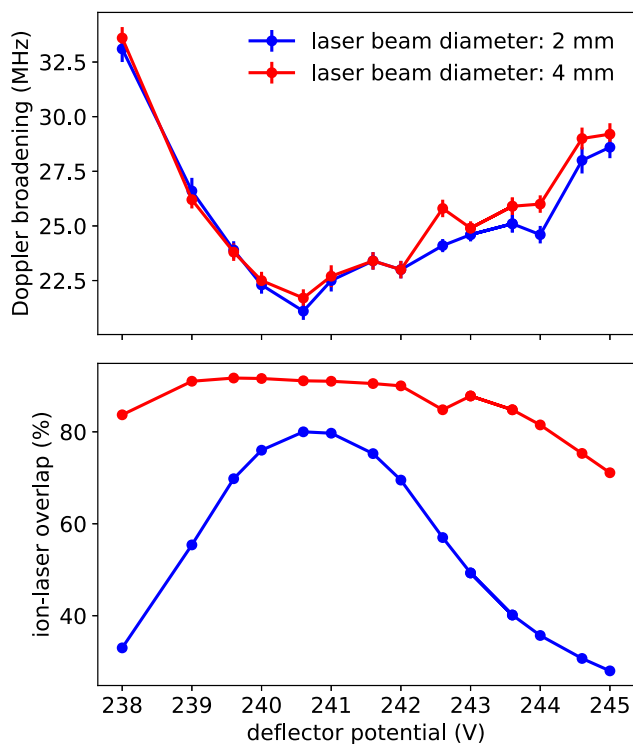


Fig. 4. Doppler broadening (FWHM) and ion–laser overlap for varying deflector potentials of the 30-degree bender for laser beam diameters of 2 mm and 4 mm. The points are connected to guide the eyes. Both observables are evaluated at the transversal middle plane of the MR-ToF device for 300 $^{24}\text{Mg}^+$ ions summed over 100 revolutions.

The reacceleration region consisting of a conical electrode leads to a focusing of the ions directly in front of the MR-ToF device. Hence the einzel lens L5 (see Fig. 1) with its large focusing strength is needed to counteract the focusing properties of the reacceleration region as well as the MR-ToF entrance mirror electrodes to provide a parallel-to-parallel ion beam injection into the MR-ToF device.

In the last optimization step, the in-trap lift potential is optimized to yield a minimal broadening of the temporal ion-bunch width. This means that the beam energy in the MR-ToF device is varied. The ideal value of the in-trap lift potential is found to be 18.85 kV. Alternatively, instead of changing the beam energy, all the potentials applied to the electrodes of the electrostatic mirrors could be scaled accordingly. The potential of the in-trap lift does not noticeably effect the Doppler broadening or ion–laser overlap, as long as most of the ions can be trapped.

The potentials obtained for the ion optical elements of the injection beamline are listed in Table 2. The potentials utilized for the einzel lenses can differ by up to 50 V from their set values without significantly altering the performance of the setup. The potentials applied to the electrodes of the 30-degree deflector are much more sensitive. Fig. 4 shows the Doppler broadening and the ion–laser overlap over the deflector potential. Details on this Doppler broadening are given in Section 5.2. Whereas the storage efficiency remains above 90% between 232 V and 245 V, the ion–laser overlap for a 2-mm laser beam diameter exceeds 70% only in a limited voltage range of 239.6 V to 242.0 V for $^{24}\text{Mg}^+$ ions. This is also the region where the Doppler broadening is minimal.

For Cd ions the potentials of the 30-degree deflector need to be changed from 240.6 V to 243.6 V for an optimal performance of the setup whereas all the other potentials can be kept the same. This small difference is due to slightly different energies which is a consequence of different Paul-trap storage and extraction settings between the two mass ranges of Mg and Cd isotopes.

Table 2

Chosen potential combination for the injection beamline electrodes with respect to the 48-kV potential of the transfer beamline. The deflector is operated with identical voltages of opposite polarity on the two plates. The optimal potential of the deflector is different for Mg and Cd isotopes.

Electrode	Potential (V)
Lens 1	−1800
Lens 2	−1400
Lens 3	−2400
Deflector	± 240.6 (Mg) or ± 243.6 (Cd)
Lens 4	−1380
Lens 5	−16950

5. Simulated performance of the setup

In this section the simulated performance of the envisioned MIRA-CLS setup will be discussed for the previously optimized potentials and geometries including the thermalization of the ions in the Paul trap, the passage of the ions along the whole transport beamline as well as their capture and storage in the MR-ToF device. 1000 ions with a selected mass between 20–34 u (Mg isotopic chain) or 96–134 u (Cd isotopic chain) are trapped in the MR-ToF instrument for 300 revolutions. In general, the simulations show that the combined injection and storage efficiency exceeds 90% and the ion–laser overlap is larger than 75% for a 2-mm laser-beam diameter. The Doppler broadening is smaller than the natural line width for all investigated isotopes with a mass between 20–34 u and 96–134 u.

In addition to the nominal case of a 50-keV ISOLDE beam and an MR-ToF device operating at 30 keV, we have also performed simulations for a 30-keV incoming ISOLDE beam, an in-trap lift of 12 kV and, thus, an 18-keV MR-ToF device. These lead to slightly worse ion–laser overlap and Doppler broadening compared to the 30-keV MR-ToF device as discussed here, but will allow high-resolution MIRACLS. In case of unexpected HV challenges, a MIRACLS operation at lower ion-beam energy is possible.

As an example, the results for $^{24}\text{Mg}^+$ ions trapped in the 30-keV MR-ToF device are discussed in the following.

5.1. Storage efficiency and ion–laser overlap

The evolution of the ion–laser overlap and that of the capture and storage efficiency as a function of revolution number are presented in Figs. 5 and 6, respectively. It typically takes a few revolutions until the ions move on trajectories in the vicinity of the axis of the MR-ToF device. About 4% of the ions are lost in the MR-ToF device during the first 7 revolutions (see Fig. 6). The ion–laser overlap fluctuates around 83% for 2-mm laser-beam diameter and around 97% for 4-mm laser-beam diameter (see Fig. 5). These estimates reflect the ion properties recorded in the transversal middle plane of the MR-ToF device. However, the spatial width of the ion bunch increases the further the ion bunch is away from the transversal middle plane of the MR-ToF device as visible in Fig. 2 (top). Hence, for a laser-beam diameter of 2 mm the ion–laser overlap decreases from 83% to 68% from the middle of the MR-ToF device to the end of the optical detection region. Assuming a laser-beam diameter of 4 mm, the ion–laser overlap is reduced from 97% in the middle to 95% at the edges of the optical detection region. The visible oscillations of ion–laser overlap versus revolution number are attributed to the periodic movement of certain ions, moving in and out from the area where they can be excited by the laser beam (see also Fig. 6 in Ref. [15]). Overall, the simulated capture and storage efficiency as well as the ion–laser overlap allow to excite most of the ions.

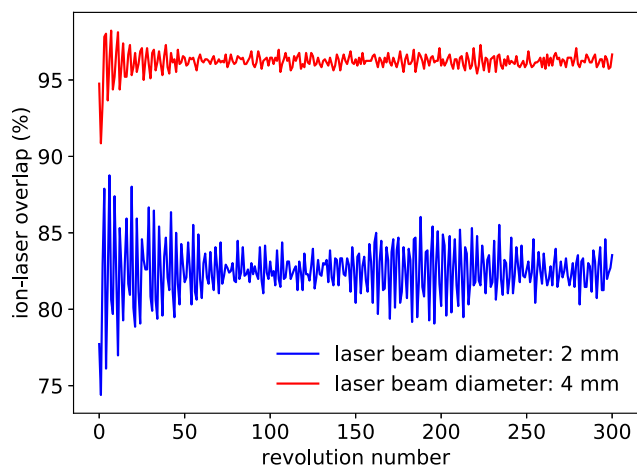


Fig. 5. Ion-laser overlap versus revolution number for 1000 $^{24}\text{Mg}^+$ ions for a laser-beam diameter of 2 mm (blue) and for 4 mm (red). Both are evaluated at the transversal middle plane of the MR-ToF device.

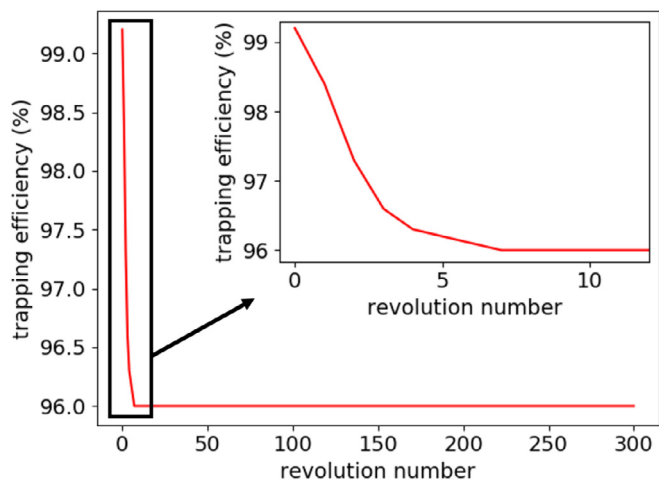


Fig. 6. Capturing and storage efficiency versus revolution number for 1000 $^{24}\text{Mg}^+$ ions. The efficiency is calculated as the fraction of ions that remain passing the middle plane of the MR-ToF during every revolution.

5.2. CLS spectra

In a classical fluorescence-based CLS experiment, the number of fluorescence photons is counted as a function of the laser frequency to obtain a (hyper)fine spectrum of the selected optical transition. To simulate the resonance spectrum of the D2 transition in Mg, the Doppler-shifted frequencies f are calculated in the laboratory frame based on the velocity of individual ions and the angles between an individual ion path and the laser beam axis according to Eq. (1). For the simulated 1000 $^{24}\text{Mg}^+$ ions, a histogram of the Doppler-shifted frequencies of the D2 transition summed over 300 revolutions is shown in Fig. 7. The natural line width is neglected in this simulation in order to clearly distinguish the different contributions to the experimental line-width broadenings. A histogram of the angles α between an individual ion trajectory and laser-beam axis, summed over all revolutions and ions, is depicted in Fig. 8. Note that the mean ion trajectory is fully aligned with the laser-beam axis. The centroid angle is 0.08 degrees and the FWHM is 0.12 degrees.

A histogram of the kinetic energy of the ions' first passage through the middle plane of the MR-ToF device can be seen in Fig. 9. Due to the energy spread of 0.82(3) eV FWHM and the angles between ions' trajectories and laser beam, the Doppler broadening is found

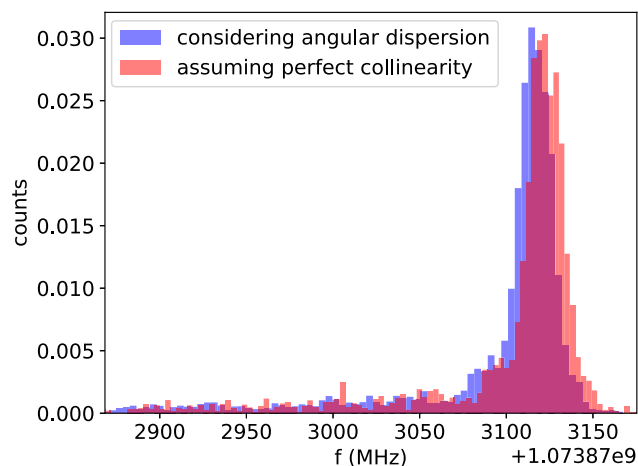


Fig. 7. Doppler-shifted frequency f of the D2 line in $^{24}\text{Mg}^+$ ions in a collinear configuration. Data is recorded at the transversal middle plane of the MR-ToF device for 1000 $^{24}\text{Mg}^+$ ions summed over 300 revolutions. In the evaluation of f for the histogram assuming perfect collinearity, the angles α are set to 0 to distinguish the effects of kinetic energy spread and angular spread on the CLS spectra. The overlapping region between the two histograms is shown in purple. The natural line width is neglected in this simulation.

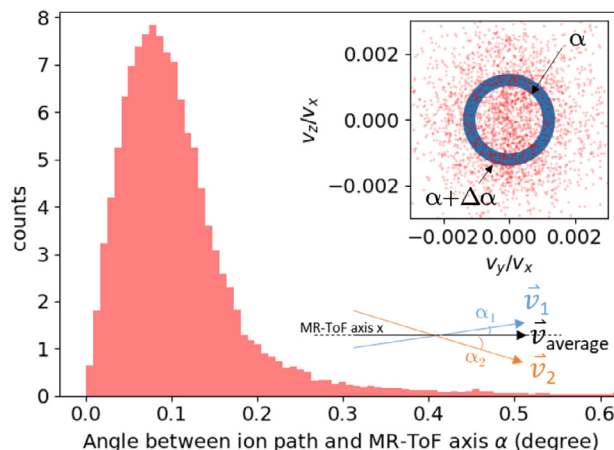


Fig. 8. Angles α between ion path and MR-ToF axis evaluated at the transversal middle plane of the MR-ToF device for 1000 $^{24}\text{Mg}^+$ ions summed over 300 revolutions. The top inset shows the ratio of the respective transversal velocity component v_y and v_z and the longitudinal velocity component v_x . Each point corresponds to one ion passing the central drift tube for revolution numbers 200–202. Because of $v_{y,z} \ll v_x$, the angle α (in mrad) can be visualized in this figure by using the approximation $\alpha^2 \approx v_y^2/v_x^2 + v_z^2/v_x^2$. The bottom inset shows two trajectories of ions with velocity \vec{v}_1 and \vec{v}_2 , that are moving with angles α_1 and α_2 in respect to the MR-ToF axis. Note that the average ion trajectory \vec{v}_{average} is fully aligned with the laser-beam axis.

to be 22.1(6) MHz for the ions excitable by a laser beam with 2-mm diameter and 23.1(6) MHz when all trapped ions are considered. According to Eq. (1), non-vanishing angles between ion trajectories and laser-beam axis will always shift the laser frequency observed in the ions' rest frame in one direction, i.e. to lower values for the collinear configuration compared to a shift to higher frequency in an anti-collinear setup. This results in a shift of the average Doppler-shifted frequency accounting to around 7.5 MHz, see Fig. 7. Note that this shift is also present when exclusively considering the first passage through the optical detection region as it would be the case in conventional CLS. Such a 7.5-MHz shift in the absolute frequency of the centroid can be neglected when isotope shifts are measured using CLS since all measured isotopes are shifted by (almost) the same amount. In the present simulation, this is verified along the isotopic chains of the Mg

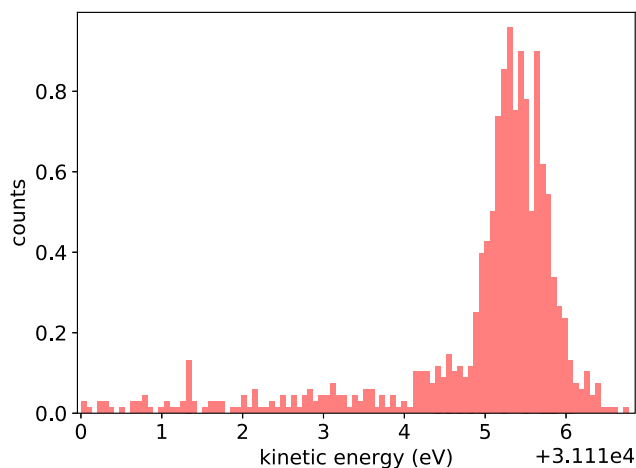


Fig. 9. Kinetic energy evaluated at the transversal middle plane of the MR-ToF device for 1000 $^{24}\text{Mg}^+$ ions for the very first passage.

and Cd ions, where any isotopic dependence is found to be less than 0.1 MHz.

The leading contribution to the asymmetric frequency lineshape, especially in the tail towards lower frequencies as depicted in Fig. 7, is shown to arise from reheating effects in the Paul trap. Some ions undergo collisions with buffer gas during extraction and reacceleration from the Paul trap and hence experience a reduction of their kinetic energy (see Fig. 9). The resulting tail in the CLS frequency spectrum is thus not specific to the MIRACLS measurement concept but a general feature of the ion preparation in buffer-gas-filled Paul traps for CLS with bunched ion beams. The asymmetry, which is arising from the angular distribution of the ions, is minimal. This can be seen in Fig. 7 where a spectrum including the effect of angular dispersion is compared with a spectrum that is assuming perfect collinearity.

Since the centroid of the Doppler-shifted resonance frequency as well as the Doppler broadening stay constant over revolution number, the CLS spectrum characteristics for 300 revolutions in the MR-ToF device are very similar to the first passage. This provides confidence that line-shape distortions due to the reflections at the mirror electrodes are well under control once the mirror potentials and ion optics for the injection into the MR-ToF device are appropriately chosen.

5.3. Evolution of the ion-bunch width

To reduce the influence of background originating from laser stray light or detector dark counts, current state-of-the-art CLS experiments employ bunched ion beams [2,6]. Photon signals are only accepted when the ion bunch is within the optical detection region such that a time-gated spectrum is obtained. Hence, it is of advantage to preserve the bunched structure of the beam over thousands of revolutions in the MIRACLS approach. In the present investigation we thus enforced the ion bunch to never become larger than half of the revolution period, i.e. 2.3 μs to 3.0 μs for Mg isotopes and 5.0 μs to 5.9 μs for Cd isotopes to still maintain a bunched beam structure. The given ranges are due to the mass dependence of the revolution period. The increase in ion-bunch width over revolution number can be described by the dispersion per turn and is desired to be as small as possible. For fixed mirror potentials and MR-ToF geometry, this is achieved by selecting an appropriate in-trap lift potential [52]. Due to limited computing resources, only a few hundred revolutions can be simulated with sufficient accuracy (see Appendix). In order to estimate the ion bunch width after many thousands of revolutions, the flight times of the ions in the MR-ToF apparatus are evaluated with respect to the time they first cross the transversal middle plane of the MR-ToF device. The ions are trapped for 100 revolutions and the resulting time spread

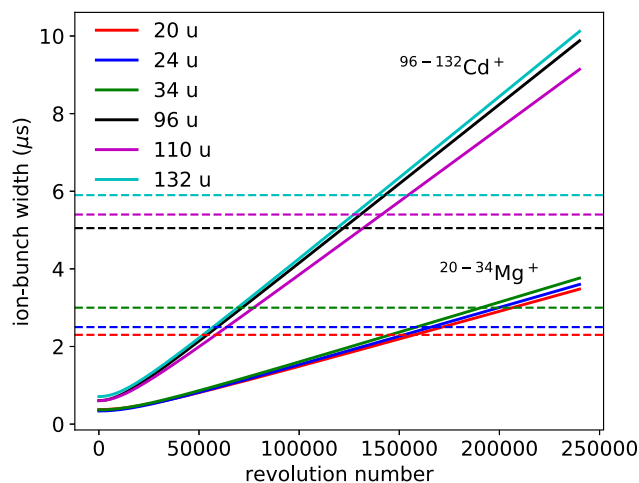


Fig. 10. Ion-bunch width (FWHM) versus revolution number for 1000 ions of various masses. To maintain the bunched ion-beam structure in the MR-ToF device the ToF peak width should remain below half of the revolution period which is indicated by horizontal lines for the different masses.

after 100 revolutions is divided by the revolution number to obtain the dispersion per turn Δt_1 . The temporal ion bunch width Δt for a given revolution number n follows as [26]

$$\Delta t = \sqrt{\Delta t_0^2 + n\Delta t_1^2}, \quad (2)$$

where Δt_0 is the initial bunch width when the ions pass the transversal middle plane for the first time. The in-trap lift potential is scanned across a broad voltage range until the region with minimal dispersion per turn is found. The evolution of the ion bunch width as a function of revolution number is shown in Fig. 10 for Mg and Cd ions.

For Mg^+ ions the bunched-beam structure is maintained until 150,000 to 190,000 revolutions depending on the isotope, corresponding to a total trapping time of 690 ms to 1.1 s. The half-lives of $^{20,21}\text{Mg}$ are around 100 ms and the half-lives of $^{30-34}\text{Mg}$ range from 313 ms down to 20 ms [66]. They are significantly shorter than the maximal trapping time given by the loss of the bunched-beam structure.

Similarly, Cd ions keep a suitable bunch structure for 120,000 to 138,000 revolutions and hence for 1.2 to 1.6 s. The Cd isotopes around the $N=82$ neutron shell closures have half-lives of a few tens of ms [66] and the majority of the trapped ions is hence decayed before the bunched-beam structure is lost. Cd isotopes around the $N=50$ neutron shell closure have half-lives in the order of a few seconds [66] and consequently lose their bunched structure before the onset of significant radioactive losses. Based on these results, we conclude that the bunched-beam structure can be maintained over many thousands of revolutions for the first science cases allowing a significant improvement in sensitivity of the MIRACLS approach in comparison to traditional single-passage CLS.

5.4. Investigation of high-voltage instabilities

In order to extend the reach of the MIRACLS technique towards more exotic radionuclides, sufficient photon counts need to be accumulated over time to unambiguously locate the CLS resonance. Hence, after the measurement of one ion bunch over thousands of revolutions in the MR-ToF device, this bunch will be released and can be recorded at an ion detector behind the MR-ToF device for e.g. intensity calibration. Moreover, in the case of very rarely produced radionuclides, the data of this ion detector could in future applications be utilized to discard any measurement cycle in which no ion of interest is trapped in the MR-ToF device and, thus, to further decrease the photon background in the analysis. To this end, the ion beam needs to be guided onto an ion

detector positioned off-centred and away from the laser beam, either by the deflector electrodes in the MR-ToF device or additional ones downstream of the electrostatic mirror. Due to the MR-ToF capability to mass separate isobars, the ions of interest can in many cases be distinguished from contaminants. Subsequently, the next ion bunch will be injected into the MR-ToF device and the measurement will be repeated ideally under exactly the same experimental conditions. However, any drift or fluctuation in the potentials applied to the Paul trap extraction, the in-trap lift or MR-ToF mirror electrodes, can alter the kinetic energy of the ions and can hence lead to a shift of the CLS centroid frequency or to a broadening of the spectral line.

Commercially available power supplies suitable for the proposed system provide peak-to-peak voltage stabilities $\Delta V/V < 10^{-5}$ within 8 h and residual ripples of less than $10^{-5} \cdot V + 10$ mV, where V is the maximal voltage of the anticipated power supplies, i.e. 35 or 65 kV depending on the potential of the respective electrode in the MIRACLS apparatus. We expect to have three different types of voltage fluctuations, those on a time scale much below the revolution period of the MR-ToF device, those on the time scale of a few revolutions in the MR-ToF device as e.g. 50-Hz electrical pick-up and those on a time scale larger than the full measurement cycle.

The latter can be addressed by regular reference scans. Thus, corrections can be made such that voltage drifts over a time period of a few hours are well under control, similarly as for traditional CLS. However, the other two types representing short-term voltage fluctuations can significantly reduce the performance of the setup.

To estimate the reduction in CLS performance due to these, the potentials of the individual mirror electrodes in the simulations are changed every time step while the ions are trapped in the MR-ToF device, either by adding Gaussian white noise or sinusoidal pick-up to the MR-ToF mirror potentials.

The Gaussian white noise is implemented via the polar form of the Box–Muller transformation [67] with a standard deviation of 0.15, 0.25 and 0.5 V. Note that since each ion is simulated independently and the potentials are changed for each ion, individual ions experience different fields during their flight time. Neither the storage efficiency nor the ion–laser overlap are found to be influenced by the added instabilities. No significant increase of temporal ion-bunch width over revolution number is observed when Gaussian white noise with up to 0.25 V standard deviation is added to the individual potentials of the mirror electrodes.

While there is hardly any visible difference for the centroid frequency, the Doppler broadening starts increasing over revolution number as visible in Fig. 11. Because of the statistical nature of this process, the linewidth may temporarily even decrease as visible, for instance, between revolution number 140 and 180 for the shown simulation considering fluctuations with a standard deviation of 0.5 V. Thus, in the scenario of a 0.15-V standard deviation, which is slightly exceeding the quoted peak-to-peak voltage fluctuations of available power supplies, 20 independent simulations are carried out and the worst case over 300 revolution is considered. This highest increase of Doppler broadening is found to be 0.009 MHz per revolution. Hence, high-resolution CLS measurements up to a few thousand revolutions are expected to be possible without any significant reduction in performance of the setup.

The sinusoidal pick-up is implemented with an amplitude of 0.4 V and frequencies between 50 Hz and 200 kHz. The amplitude is motivated by the expected residual ripples of the MR-ToF mirror power supplies. Arbitrary phases between the individual mirror electrodes are assumed, including the case in which the sinusoidal pick-up has the same phase for all electrodes. Neither the storage efficiency nor the ion–laser overlap are influenced by the instabilities described above. The centroid frequency follows the sinusoidal behaviour of the mirror potentials (see Fig. 12 for some selected frequencies), while the Doppler broadening is nearly constant. As long as the sinusoidal period is longer than the revolution period and hence the frequency smaller than 200 kHz, the peak-to-peak changes in resonance centroid are the same

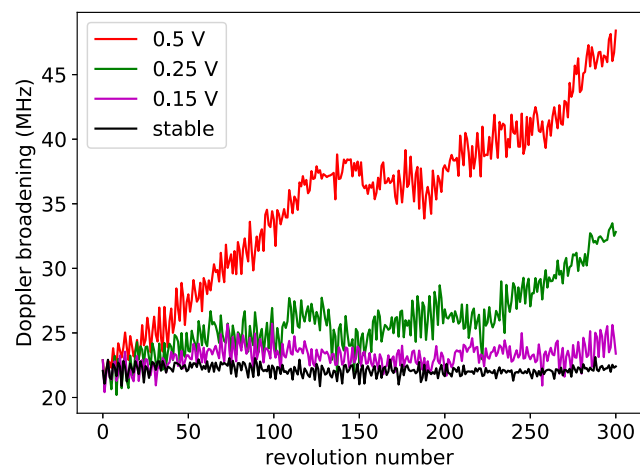


Fig. 11. Doppler broadening (FWHM) versus revolution number for the addition of Gaussian white noise to the potentials of the MR-ToF mirror electrodes. Only ions excitable by a laser with 2-mm beam diameter are taken into account when 300 $^{24}\text{Mg}^+$ ions are evaluated at the transversal middle plane of the MR-ToF device. The consequences are studied for Gaussian white noise with different standard deviations.

and in the order of 8 MHz for the tested frequencies and phases. This is also found when a multiple of the revolution period T is chosen for the sinusoidal period. Due to the fact that the photon signal of all revolutions are added up, a broadening of the line shape will occur, which is expected to be in the order of 8 MHz.

While for ions within the same ion bunch the phase of the sinusoidal pick-up is always the same, in the experiment the photon signals of more ion bunches will be added up to improve statistics and hence an additional broadening of the line shape will occur in the experiment. This broadening will be smaller than the natural line width up to a few 1000 revolutions and hence high-resolution CLS measurements are expected to be possible even without additional stabilization of the power supplies.

Voltage fluctuations of the potentials applied to the Paul trap extraction electrodes as well as to the central drift tube of the MR-ToF device can lead to a broadening of the line shape or a shift in centroid frequency. Both are however also present in traditional CLS measurements and are thus not expected to degrade the MIRACLS performance in comparison to the conventional technique.

If the stability of the power supplies is unexpectedly worse than their manufacturer's specifications, similar stabilization techniques as discussed in [68–70] can be applied to the 30-keV MR-ToF device power supplies to minimize the increase in Doppler broadening.

5.5. Modelling of a realistic in-trap lift switching

Up to this point an ideal high-voltage (HV) switching for the operation of the in-trap lift is assumed, e.g. instantaneous switching from 18.85 kV to ground potential. However, any real HV switch circuit exhibits a non-vanishing time constant in the switching process. To investigate the influence of a realistic HV switch circuit on the performance of MIRACLS, we employ two different circuit models to obtain electrode response functions which can qualitatively describe the trend in the transient behaviour. Firstly, the voltage behaviour over time is measured for the in-trap lift switch used at the 1.5-keV MR-ToF device with $U_l = 700$ V in MIRACLS' proof-of-principle experiment [18,19] and scaled to $U_l = 18.85$ kV. Secondly, electronic circuit simulations for a simplified model of the in-trap lift switch of the 30-keV MR-ToF device are performed with the software LTspice [71]. To obtain response functions that can be used in SimIon, the potential curves $U(t)$ are fitted with the following function for both models:

$$U(t) = \begin{cases} U_l & \text{for } t < 0 \\ U_l \cdot (a \cdot e^{-t/t_f} + (1-a) \cdot e^{-t/t_s}) & \text{for } t > 0, \end{cases} \quad (3)$$

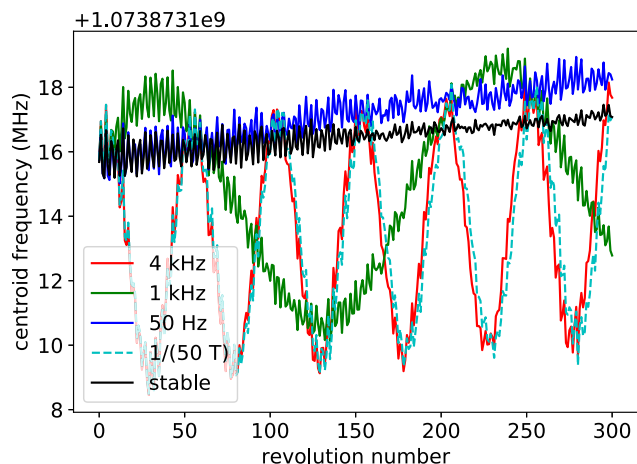


Fig. 12. CLS centroid frequency versus revolution number for the application of sinusoidal voltage variations for 300 $^{24}\text{Mg}^+$ ions evaluated at the transversal middle plane of the MR-ToF device. Sinusoidal voltage fluctuations of 0.4 V amplitude with different frequencies are added to the potentials of the individual MR-ToF mirror electrodes. The dashed light-blue line shows the case when the sinusoidal period is given by the revolution period T multiplied with a factor of 50. The slight increase in centroid frequency over revolution number is explained by the chosen geometrical resolution in this simulation, see [Appendix](#).

Table 3

Fit constants as used for the modelling of the high voltage switch, as defined in Eq. (3). The second column (measured) shows the parameters for the in-trap lift at the MIRACLS proof-of-principle experiment, which are measured for $U_l = 700$ V and scaled to $U_l = 18.85$ kV. The third column (simulated) lists the parameters for the planned HV switch configuration for the 30-keV MR-ToF device simulated in LTspice. See text for details.

Parameter	Measured	Simulated
a	0.992549	1
t_f	45.8 ns	42.6 ns
t_s	12.84 μs	–

The respective fit parameters a, t_f, t_s can be found in [Table 3](#) and the different switch functions are compared to each other in [Fig. 13](#). We assume two time constants t_s and t_f . The fast component $a \cdot e^{-t/t_f}$ is very similar between scaled measurement and LTspice simulation. However, the scaled measurement shows an additional slow component $(1 - a) \cdot e^{-t/t_s}$ which is not present in the LTspice simulations. The most likely explanation to the observed difference is the incomplete description of the internal structure of the commercial switch in the simulations and the resulting uncertainty on the involved electrical parasitics.

On closer inspection of the simulated centroid frequency and Doppler broadening over revolution number for 100 $^{24}\text{Mg}^+$ ions (see [Fig. 14](#)) no noticeable differences between the ideal switch and the switch simulated in LTspice are observed. For the measurement-based response function, it takes up to 20 revolutions until a stable centroid frequency and Doppler broadening are reached. This is a consequence of the slow component in the HV switching of the in-trap lift potential. Moreover, the centroid frequency and Doppler broadening are significantly larger for the measurement-based switching function compared to the ideal switch as shown in [Fig. 14](#). Within the first 20 revolutions the ions see different potentials of the central drift tube for each revolution, which causes changes in the kinetic energy of the ions over revolution number and hence a change in centroid frequency of almost 2 GHz. When assuming the measurement-based response function, the Doppler broadening accounts for around 42.5 MHz which is in the order of the natural line width. Hence, high-resolution CLS is also possible with the measurement-based in-trap lift switching function.

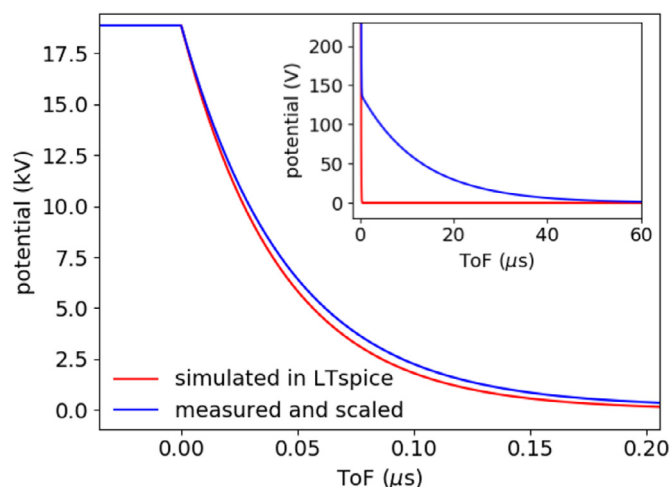


Fig. 13. Different models for the HV switching of the central drift tube are compared. Blue curve: The voltage behaviour over time is measured for the in-trap lift switch used at the MIRACLS proof-of-principle 1.5-keV MR-ToF device and the result is scaled to $U_l = 18.85$ kV. Red curve: LTspice simulations are performed for the components to be used in the planned configuration of the in-trap lift switch for the 30-keV MR-ToF device. The inset shows a low-voltage region for several tens of microseconds.

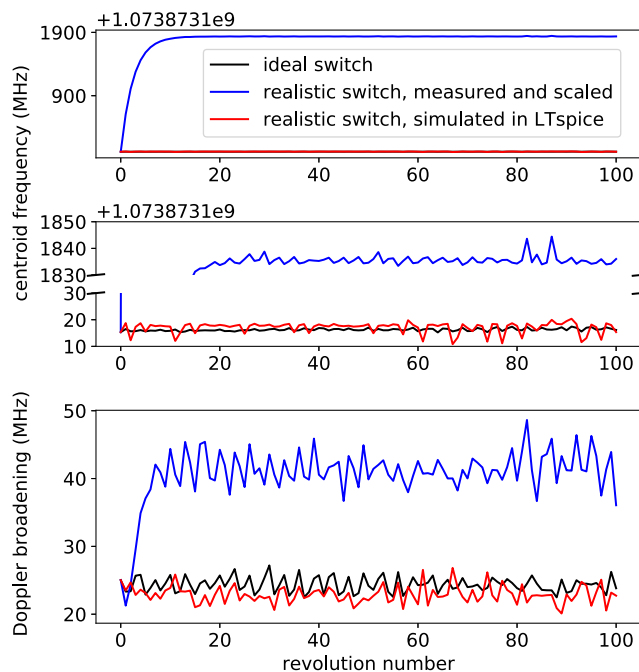


Fig. 14. (Top) Simulated CLS centroid frequency versus revolution number for 100 $^{24}\text{Mg}^+$ ions evaluated at the transversal middle plane of the MR-ToF device for different potential-over-time functions of the in-trap lift switch. In the case of the ideal switch the simulation is done with 1000 $^{24}\text{Mg}^+$ ions. (Middle) A zoom of the top panel. (Bottom) Doppler broadening (FWHM) versus revolution number taking only ions excitable by a laser with 2-mm beam diameter into account for different in-trap lift switching functions. The ions need around 5.05 μs to complete one revolution.

The ions' kinetic energy after 20 revolutions (corresponding to a storage time of around 100 μs) is approximately 62 eV larger for the measured and scaled in-trap lift switch compared to the ideal case. To obtain the isotope shifts from the experimental data, the measured Doppler-shifted resonance frequencies f in the laboratory frame as shown in, e.g., [Fig. 14](#) need to be converted to the resonance frequencies f_0 in the rest frame of the ions. This can be done via equation (1) with $\alpha = 0$. As usually the case in the analysis of CLS data, the ions

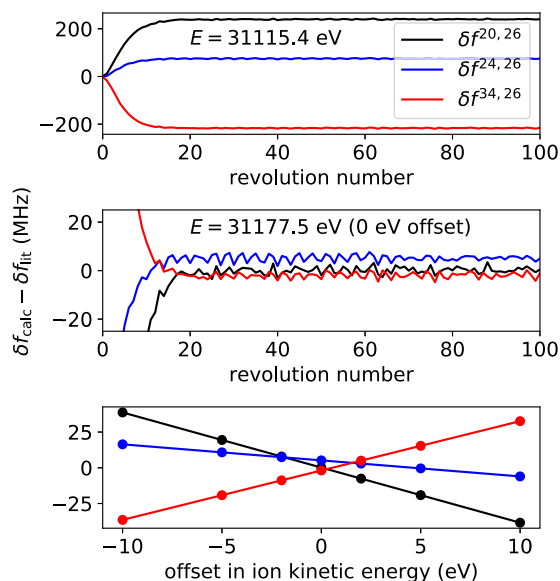


Fig. 15. Difference between the calculated isotope shift δf_{calc} and the (extrapolated) literature value [33,72] δf_{lit} for different assumed ion energies in the determination of δf_{calc} in the D1 line. The top figure shows this difference versus revolution number for $^{20,24,34}\text{Mg}^+$ vs $^{26}\text{Mg}^+$ ions if the determination of the beam energy assumes an ideal in-trap lift switch ($E = 31115.4$ eV), while the actual ion energy is governed by a realistic HV switching. The middle figure shows the isotope shift difference as function of revolution number for the actual energy $E = 31177.5$ eV which the ions end up to have after 25 revolutions in the simulations. The bottom figure shows the mean difference in isotope-shift determination versus offset from the actual energy $E = 31177.5$ eV, taking all revolutions between 25 and 100 into account. As switching function for the in-trap lift, the measurement-based switching behaviour is used. See text for details.

are assumed to move fully parallel to the laser beam axis, hence $\alpha = 0$, since the angles of individual ion trajectories are not experimentally accessible. The velocity of the ions v is given by

$$v = c \sqrt{1 - \frac{m^2 c^4}{(E + mc^2)^2}} \quad (4)$$

with E the energy and m the mass of the ions.

The calculation of the rest frame frequencies requires precise knowledge of the ions' energy. For a switch with a slow time constant, the ions' energy is a priori not well known and can lead to systematic deviations in the order of up to a few 100 MHz in isotope-shift measurements [19]. Indeed, by assuming the ion kinetic energy that the ions would have in case of an ideal lift switching, one would make a systematic error of up to 240 MHz between $^{20,24,34}\text{Mg}^+$ versus $^{26}\text{Mg}^+$ as shown in Fig. 15 (top).

When using the actual ion kinetic energy that the ions have after 25 revolutions in the simulations and when neglecting the first 20 revolutions we have systematic deviations of less than 5 MHz in the simulated isotope shifts between $^{20,24,34}\text{Mg}^+$ versus $^{26}\text{Mg}^+$ as shown in Fig. 15 (middle). Fig. 15 (bottom) shows the systematic error in the isotope shift for different offsets in the assumed ion energy compared to its literature value. A 5-eV offset in ion kinetic energy leads to a systematic error of up to 20 MHz.

If the transient behaviour of the in-trap lift switch circuit is well understood, the shift in energy due to the realistic HV switching could in principle be corrected in the analysis of the isotope shift. However, in practice an accurate characterization of a fast 20-kV HV switch remains a technical challenge which cannot be easily resolved by a purely simulation approach of the switch circuit.

For this reason, the kinetic energy after a few tens of revolutions in the MR-ToF device needs to be determined by other means. Once the kinetic energy is known for one isotope it can be used for the isotope

Table 4

Expected line width broadenings for MIRACLs measurements of the D1 and D2 line in Mg^+ ions. See text for details.

Cause of broadening	Broadening (MHz)
Natural line width	42
Doppler broadening (depending on in-trap lift switching behaviour)	23–42.5
Gaussian white noise on mirror electrodes	<0.009 MHz per revolution
Sinusoidal noise on mirror electrodes	<8
Total (5000 revolutions)	<75
Total (10,000 revolutions)	<108

shift calculation along the entire isotopic chain as long as there are no additional energy shifts between the individual isotopes, as holds true in the simulations. The beam energy can also be determined via CLS measurements: The very precisely measured resonance frequencies f_0 of the D1 and D2 line in the ions' rest frame of either $^{24}\text{Mg}^+$ or $^{26}\text{Mg}^+$ ions can be taken from literature [72]. The kinetic energy can then be calculated according to Eq. (1) from the measured resonance frequency in the laboratory frame of the respective stable isotope. Alternatively, one can determine the rest frame transition frequency f_0 via collinear and anticollinear measurements performed on one specific isotope within the MIRACLs apparatus itself. Once f_0 is known it can be used to determine the beam energy in combination with any collinear or anticollinear measurement carried out at later times. If the same wavemeter for measuring the laser frequency is used, the wavemeter uncertainty is almost eliminated and the beam energy can be determined with a relative uncertainty of 10^{-5} [73]. This would correspond to around 0.3 eV at MIRACLs which is a sufficiently accurate estimation of the experimental ion beam energy for MIRACLs, see Fig. 15 (bottom).

We note that the timing between Paul trap extraction and switching of the in-trap lift needs to be adjusted for each individual isotope, such that the isotope of interest is within the field-free region when the lift is switched for trapping. In the following it is investigated for one specific isotope, namely $^{24}\text{Mg}^+$, how the energy is changed when the ion of interest is not exactly in the middle of the in-trap lift when its HV switching for trapping takes place. In the case of the measurement-based switching function, a 0.1- μs offset in the switch timing leads to an offset in the energy of 0.5 eV, corresponding to a systematic error of 16 MHz in the D1 line of Mg (see Fig. 16). In the case of the simulated switch circuit in LTspice, a 0.1- μs offset switch timing just changes the centroid energy by 0.15 eV, corresponding to a systematic error of 4.5 MHz. The change in the centroid energy due to the offset switch timing is in the simulations observed to be mass independent in a range from 20 to 134 u. Provided careful adjustment of the in-trap lift switch timing for each isotope, no significant systematic deviations are expected in CLS measurements at MIRACLs. Appropriate timings can be deduced from the ions' ToF spectra as recorded on a MagneToF detector downstream of the MR-ToF device. Once known for one mass, a scaling to other isotopes is feasible. We investigate this effect nevertheless since there might be (small) uncertainties in the scaling or inaccuracies in the timing signals.

In Table 4 a short summary of the expected line broadenings as relevant for the MIRACLs technique is given, while Table 5 lists the expected systematic deviations on the isotope shift.

The systematic error on the isotope shift arising due to a limited knowledge on the kinetic energy on the 5-eV level is less than 20 MHz. If the switch timing is oppositely offset by 0.1 μs for both isotopes or if it is offset for only one isotope by 0.2 μs a systematic error of 32 MHz originates. This results in a total systematic error of 38 MHz for a future measurement of the isotope shift of ^{20}Mg to ^{34}Mg in the most conservative application of MIRACLs. This is comparable in magnitude to systematic uncertainties of previous measurements on exotic Mg isotopes [33]. More recent work in traditional, single-passage CLS reports systematic errors for isotope shifts over the same mass

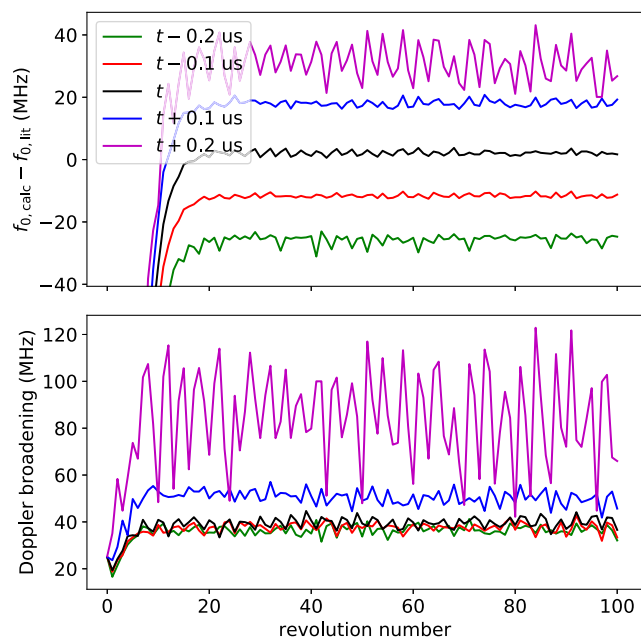


Fig. 16. (Top) Difference between the calculated resonance frequency in the ions' rest frame according to Eq. (1) and the literature value [72] versus revolution number for 100 $^{24}\text{Mg}^+$ ions in the D1 line. The simulations are evaluated at the transversal middle plane of the MR-ToF device for different timings between Paul trap extraction and in-trap lift switching. At time t the ion bunch is exactly in the middle of the central drift tube, when the HV switching is activated. (Bottom) Doppler broadening (FWHM) versus revolution number taking only ions excitable by a laser with 2-mm beam diameter into account for different timings between Paul trap extraction and in-trap lift switching. The measurement-based function for the in-trap lift switch is used.

Table 5

Simulated upper limit of the investigated systematic deviations of the MIRACLs technique on the isotope shifts for Mg^+ ions of mass $A = 20\text{--}34$ versus ^{26}Mg . Note that the limited knowledge of the beam energy is both given by the Paul trap acceleration potential as well as by the realistic HV switching of the in-trap lift of the MR-ToF device. By performing simultaneous collinear–anticollinear measurements the systematic error due to the ion energy is eliminated. See text for details.

Cause of error	Uncertainty on isotope shift (MHz)
Limited knowledge of energy on 5-eV level	20
Non-ideal switch timings of in-trap lift	32

difference by a factor of 2 to 10 smaller, e.g. [37,74–77]. There, they are related to the uncertainty of the acceleration potential. Given that an offset in acceleration potential equally effects the kinetic energy of all studied isotopes, an uncertainty in its determination leads to errors in the isotope shifts which are correlated along the entire isotopic chain and increase in size as function of the mass difference to the reference ion. This effect is common to both, MIRACLs as well as traditional single-passage CLS. If absolute, nuclear charge radii are known for at least three isotopes along the studied isotopic chain, a King-plot analysis can be performed. As a result, the systematic error due to incomplete knowledge of the acceleration potential is eliminated in the determination of the other charge radii from the measured isotope shifts.

For MIRACLs, however, an additional systematic error arises due to inaccurate settings in the timings of the HV switching. This can lead to shifts in resonance-centroid frequencies which may vary in size and direction from isotope to isotope and which are not eliminated in the extraction of charge radii via a King-plot analysis. In order to minimize this effect, the consequences of the switch timing on the isotope shift will be studied for the well-known (stable) isotopes before an online experiment. Moreover, the correct switch timings can be precisely determined for abundant (stable) ion species and, then, scaled to its

value for an exotic nuclide. Thus, within the systematic uncertainties estimated above, we do not expect any significant reduction in the performance or accuracy of the MIRACLs technique even when a slow in-trap lift switching is employed.

Finally, if simultaneous collinear–anticollinear laser spectroscopy measurements are performed, the uncertainties on the ions' energies are eliminated [78]. Due to the trapping of the ions in the MR-ToF device, collinear and anticollinear probing of the ions can be done within the same measurement and hence no additional time is required, provided a second laser system is available.

6. Conclusion and outlook

The simulation of CLS in the envisioned 30-keV MR-ToF apparatus in combination with the first experimental results of MIRACLs' proof-of-principle experiment [15–19] demonstrate the feasibility of high-resolution CLS in an MR-ToF device and highlight the potential of the novel concept of MIRACLs. Building on the successful benchmarking of the simulation approach against the experimental 1.5-keV proof-of-principle data, extensive simulations of the new 30-keV device and its injection optics have been performed in the present work. Taking the space constraints in the ISOLDE experimental hall into account, suitable geometries and potentials for ion beam preparation and transfer as well as MR-ToF injection and operation have been found.

These allow for > 90% injection and storage efficiency, > 75% ion–laser overlap and a line width approaching the natural line width of the transition of interest. When the electrostatic potentials applied to the MR-ToF mirror electrodes and ion optical elements of the transport beamline are optimized for the requirements of CLS, the shape of the simulated spectral line is neither significantly broadened nor distorted by the combination of CLS and MR-ToF operation. Additional systematic effects such as high-voltage instabilities or non-ideal high-voltage switches do not lead to any significant reduction in performance of the MIRACLs technique in the simulations. This indicates that accuracy and resolution for MIRACLs will be close to traditional single-passage CLS. However, by trapping the ions in the 30-keV MR-ToF device the sensitivity of traditional CLS will be enhanced by more than one to two orders of magnitude.

The construction of the 30-keV MR-ToF device as simulated in this work is currently ongoing and its commissioning will be topic of a future publication. The first MIRACLs measurements are foreseen to be performed on neutron-rich Magnesium isotopes in the island of inversion and Cadmium isotopes at and beyond the $N=50$ and $N=82$ neutron shell closures. Following a similar simulation approach but focused on mass separation, we are currently investigating a 30-keV MR-ToF device with the aim to provide high purity radioactive beams to downstream experiments.

Declaration of competing interest

The authors declare that they have no known competing financial interests or personal relationships that could have appeared to influence the work reported in this paper.

Data availability

Input data and datasets generated and analysed during the current study are available from the corresponding author on request. The simulation package SimIon itself is available at <https://simion.com/>.

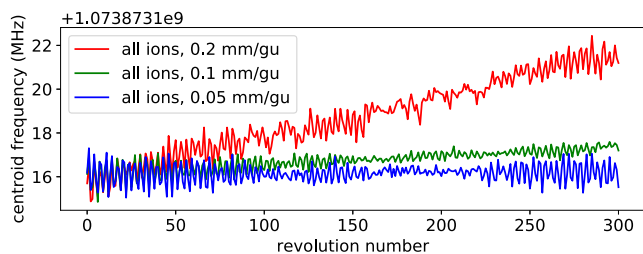


Fig. 17. Simulated CLS centroid frequency versus revolution number for 1000 $^{24}\text{Mg}^+$ ions evaluated at the transversal middle plane of the MR-ToF device for different chosen grid resolutions.

Acknowledgements

The research leading to these results has received funding from the European Research Council (ERC) under the European Union's Horizon 2020 research and innovation programme under grant agreement No. 679038. The work was additionally supported by the Canadian Natural Science and Engineering Council (NSERC). Part of the work of F.M.M. has been sponsored by the Wolfgang Gentner Programme of the German Federal Ministry of Education and Research, Germany (grant no. 05E18CHA). We are grateful for support of the MIRACLS project from CERN, Switzerland, the ISOLDE Collaboration, Switzerland, and the Max-Planck-Institut für Kernphysik (MPI K) in Heidelberg, Germany.

Appendix

To improve the accuracy in SimIon the following steps are undertaken in this work: A 3D solid geometry modelling language is used to define the respective geometries of the setup in an ASCII file with .gem extension, which can be directly read in by SimIon. A simplified model of the beamline is included in the simulations to properly define the boundary conditions of the potentials. SimIon's surface enhancement feature is enabled to better model curved surfaces.

The simulations are split into three different geometrical segments. In the simulation segments between Paul trap and Lens 4, a geometrical resolution of 0.5 mm per grid unit is used together with a convergence objective of $1e-5$ V in electric field refinement. For the final, fully cylindrical symmetric simulation segment including Lens 5 and the MR-ToF device, 0.1 mm per grid unit and $1e-7$ V are used to minimize computational errors. The maximal size of a time step is given by the time the ions need to travel one grid unit, but a dynamical reduction of its size is enabled to improve accuracy when needed, e.g. close to the electrode surfaces or during the reversal of the axial velocity of the ions in the MR-ToF device.

The ion parameters are passed on to the next simulation segment at user-defined planes, perpendicular to beam propagation, via a Python routine which is executing the respective SimIon simulations for all geometrical segments. In order to ensure smooth transitions, it is required that the adjacent segments have identical fields at the common plane. For the calculation of the ion trajectories relativistic corrections are enabled in SimIon. However, no differences are noticeable for the results presented in this work if a fully classical treatment is chosen.

When trapping the ions for multiple revolutions in the MR-ToF device computational errors may accumulate leading to significant errors after many revolutions. Hence the simulations in this work are limited to the first 300 revolutions.

The inaccuracy of the simulations for too large grid spacing is also evident by a nonphysical change of the energy of individual ions. By comparing different grid resolutions it is verified that the simulations have indeed converged as exemplary shown for the evolution of the centroid frequency and the ion-bunch width over revolution number in Figs. 17 and 18. While for a geometrical resolution of 0.2 mm per grid unit the centroid frequency increases with revolution number, the

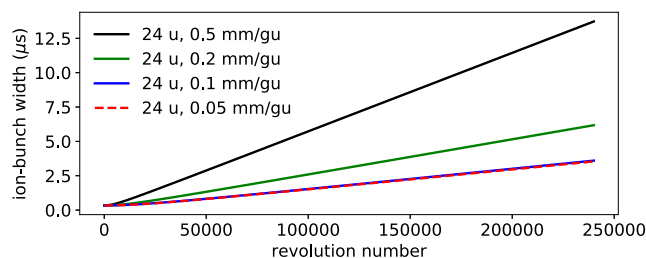


Fig. 18. Ion-bunch width (FWHM) versus revolution number for 1000 $^{24}\text{Mg}^+$ ions with various grid resolutions.

simulations using 0.1 mm per grid unit are almost constant, yielding results close to the ones for 0.05 mm per grid unit. In the case of the evolution of the ion-bunch width over revolution number 0.05 and 0.1 mm per grid unit lead to the same overall behaviour, while 0.2 and 0.5 mm per grid unit lead to a too large increase of ion-bunch width over revolution number. Hence, 0.1 mm grid spacing provides a suitable accuracy for our purposes while the setup and run times of the simulations are still kept reasonably small.

References

- [1] E.W. Otten, Nuclear radii and moments of unstable isotopes, in: *Treatise on Heavy Ion Science: Volume 8: Nuclei Far from Stability*, Springer US, Boston, MA, 1989, pp. 517–638.
- [2] B. Cheal, K.T. Flanagan, Progress in laser spectroscopy at radioactive ion beam facilities, *J. Phys. G: Nucl. Part. Phys.* 37 (11) (2010) 113101.
- [3] K. Blaum, J. Dilling, W. Nörtershäuser, Precision atomic physics techniques for nuclear physics with radioactive beams, *Phys. Scr.* 2013 (T152) (2013) 014017.
- [4] P. Campbell, I. Moore, M. Pearson, Laser spectroscopy for nuclear structure physics, *Prog. Part. Nucl. Phys.* 86 (2016) 127–180.
- [5] R. Neugart, J. Billowes, M.L. Bissell, K. Blaum, B. Cheal, K.T. Flanagan, G. Neyens, W. Nörtershäuser, D.T. Yordanov, Collinear laser spectroscopy at ISOLDE: new methods and highlights, *J. Phys. G: Nucl. Part. Phys.* 44 (6) (2017) 064002.
- [6] A. Nieminen, P. Campbell, J. Billowes, D.H. Forest, J.A.R. Griffith, J. Huikari, A. Jokinen, I.D. Moore, R. Moore, G. Tungate, J. Äystö, On-line ion cooling and bunching for collinear laser spectroscopy, *Phys. Rev. Lett.* 88 (2002) 094801.
- [7] T. Cocolios, H. Al Suradi, J. Billowes, I. Budinčević, R. de Groot, S. De Schepper, V. Fedosseev, K. Flanagan, S. Franchoo, R. Garcia Ruiz, H. Heylen, F. Le Blanc, K. Lynch, B. Marsh, P. Mason, G. Neyens, J. Papuga, T. Procter, M. Rajabali, R. Rossel, S. Rothe, G. Simpson, A. Smith, I. Strashnov, H. Stroke, D. Verney, P. Walker, K. Wendt, R. Wood, The Collinear Resonance Ionization Spectroscopy (CRIS) experimental setup at CERN-ISOLDE, *Nucl. Instrum. Methods Phys. Res. B* 317 (2013) 565–569.
- [8] R.P. de Groot, J. Billowes, C.L. Binnersley, M.L. Bissell, T.E. Cocolios, T. Day Goodacre, G.J. Farooq-Smith, D.V. Fedorov, K.T. Flanagan, S. Franchoo, R.F. Garcia Ruiz, W. Gins, J.D. Holt, Á. Koszorús, K.M. Lynch, T. Miyagi, W. Nazarewicz, G. Neyens, P.G. Reinhard, S. Rothe, H.H. Stroke, A.R. Vernon, K.D.A. Wendt, S.G. Wilkins, Z.Y. Xu, X.F. Yang, Measurement and microscopic description of odd–even staggering of charge radii of exotic copper isotopes, *Nat. Phys.* 16 (6) (2020) 620–624.
- [9] Á. Koszorús, X.F. Yang, W.G. Jiang, S.J. Novario, S.W. Bai, J. Billowes, C.L. Binnersley, M.L. Bissell, T.E. Cocolios, B.S. Cooper, R.P. de Groot, A. Ekström, K.T. Flanagan, C. Forssén, S. Franchoo, R.F.G. Ruiz, F.P. Gustafsson, G. Hagen, G.R. Jansen, A. Kanellakopoulos, M. Kortelainen, W. Nazarewicz, G. Neyens, T. Papenbrock, P.G. Reinhard, C.M. Ricketts, B.K. Sahoo, A.R. Vernon, S.G. Wilkins, Charge radii of exotic potassium isotopes challenge nuclear theory and the magic character of $N=32$, *Nat. Phys.* 17 (2021) 439–443.
- [10] R. Heinke, T. Kron, S. Raeder, T. Reich, P. Schönberg, M. Trümper, C. Weichhold, K. Wendt, High-resolution in-source laser spectroscopy in perpendicular geometry. Development and application of the PI-LIST, *Hyperfine Interact.* 238 (2017) 6.
- [11] R. Ferrer, A. Barzakh, B. Bastin, R. Beerwerth, M. Block, P. Creemers, H. Grawe, R. de Groot, P. Delahaye, X. Flécharde, S. Franchoo, S. Fritzsche, L.P. Gaffney, L. Ghys, W. Gins, C. Granados, R. Heinke, L. Hijazi, M. Huyse, T. Kron, Y. Kudryavtsev, M. Laatiaoui, N. Lemesne, M. Loiselet, F. Lutton, I.D. Moore, Y. Martínez, E. Mogilevskiy, P. Naubereit, J. Piot, S. Raeder, S. Rothe, H. Savajols, S. Sels, V. Sonnenschein, J.-C. Thomas, E. Traykov, C. Van Beveren, P. Van den Bergh, P. Van Duppen, K. Wendt, A. Zadornaya, Towards high-resolution laser ionization spectroscopy of the heaviest elements in supersonic gas jet expansion, *Nature Commun.* 8 (1) (2017) 14520.

- [12] S. Raeder, M. Block, P. Chhetri, R. Ferrer, S. Kraemer, T. Kron, M. Laatiaoui, S. Nothhelfer, F. Schneider, P. Van Duppen, M. Verlinde, E. Verstraelen, T. Walther, A. Zadornaya, A gas-jet apparatus for high-resolution laser spectroscopy on the heaviest elements at SHIP, *Nucl. Instrum. Methods Phys. Res. B* 463 (2020) 272–276.
- [13] S. Sels, F.M. Maier, M. Au, P. Fischer, C. Kanitz, V. Lagaki, S. Lechner, E. Leistschneider, D. Leimbach, E.M. Lykiardopoulou, A.A. Kwiatkowski, T. Manovitz, Y.N. Vila Gracia, G. Neyens, P. Plattner, S. Rothe, L. Schweikhard, M. Vilen, R.N. Wolf, S. Malbrunot-Ettenauer, Doppler and sympathetic cooling for the investigation of short-lived radioactive ions, *Phys. Rev. Res.* 4 (2022) 033229.
- [14] R.F.G. Ruiz, C. Gorges, M. Bissell, K. Blaum, W. Gins, H. Heylen, K. Koenig, S. Kaufmann, M. Kowalska, J. Krämer, P. Lievens, S. Malbrunot-Ettenauer, R. Neugart, G. Neyens, W. Nörtershäuser, D.T. Yordanov, X.F. Yang, Development of a sensitive setup for laser spectroscopy studies of very exotic calcium isotopes, *J. Phys. G: Nucl. Part. Phys.* 44 (4) (2017) 044003.
- [15] F.M. Maier, P. Fischer, H. Heylen, V. Lagaki, S. Lechner, P. Plattner, S. Sels, F. Wienholtz, W. Nörtershäuser, L. Schweikhard, S. Malbrunot-Ettenauer, Simulations of a proof-of-principle experiment for collinear laser spectroscopy within a multi-reflection time-of-flight device, *Hyperfine Interact.* 240 (1) (2019) 54.
- [16] S. Lechner, P. Fischer, H. Heylen, V. Lagaki, F. Maier, P. Plattner, M. Rosenbusch, S. Sels, F. Wienholtz, R.N. Wolf, W. Nörtershäuser, L. Schweikhard, S. Malbrunot-Ettenauer, Fluorescence detection as a new diagnostics tool for electrostatic ion beam traps, *Hyperfine Interact.* 240 (1) (2019) 95.
- [17] V. Lagaki, P. Fischer, H. Heylen, F. Hummer, S. Lechner, S. Sels, F. Maier, P. Plattner, M. Rosenbusch, F. Wienholtz, R. Wolf, W. Nörtershäuser, L. Schweikhard, S. Malbrunot-Ettenauer, Stray-light suppression for the MIRACLS proof-of-principle experiment, *Acta Phys. Polon. B* 51 (2020) 571–576.
- [18] S. Sels, P. Fischer, H. Heylen, V. Lagaki, S. Lechner, F. Maier, P. Plattner, M. Rosenbusch, F. Wienholtz, R. Wolf, W. Nörtershäuser, L. Schweikhard, S. Malbrunot-Ettenauer, First steps in the development of the Multi Ion Reflection Apparatus for Collinear Laser Spectroscopy, *Nucl. Instrum. Methods Phys. Res. B* 463 (2020) 310–314.
- [19] V. Lagaki, H. Heylen, I. Belosevic, P. Fischer, C. Kanitz, S. Lechner, F. Maier, W. Nörtershäuser, P. Plattner, M. Rosenbusch, S. Sels, L. Schweikhard, M. Vilen, F. Wienholtz, R. Wolf, S. Malbrunot-Ettenauer, An accuracy benchmark of the MIRACLS apparatus: Conventional, single-passage collinear laser spectroscopy inside a MR-ToF device, *Nucl. Instrum. Methods Phys. Res. A* 1014 (2021) 165663.
- [20] F.M. Maier, Laser Spectroscopy of Short-Lived Radionuclides in an Ion Trap: MIRACLS' Proof-of-Principle Experiment and the Simulation of the Future 30-keV MR-ToF Device (M.Sc. thesis), Johannes Kepler University Linz, 2019.
- [21] A. Piechaczek, V. Shchepunov, H.K. Carter, J.C. Batchelder, E.F. Zganjar, S.N. Liddick, H. Wollnik, Y. Hu, B.O. Griffith, Development of a high resolution isobar separator for study of exotic decays, *Nucl. Instrum. Methods Phys. Res. B* 266 (19) (2008) 4510–4514.
- [22] W.R. Plaß, T. Dickel, U. Czok, H. Geissel, M. Petrick, K. Reinheimer, C. Scheidenberger, M. I.Yavor, Isobar separation by time-of-flight mass spectrometry for low-energy radioactive ion beam facilities, *Nucl. Instrum. Methods Phys. Res. B* 266 (19–20) (2008) 4560–4564.
- [23] P. Schury, K. Okada, S. Shchepunov, T. Sonoda, A. Takamine, M. Wada, H. Wollnik, Y. Yamazaki, Multi-reflection time-of-flight mass spectrograph for short-lived radioactive ions, *Eur. Phys. J. B* 42 (3) (2009) 343.
- [24] F. Wienholtz, D. Beck, K. Blaum, C. Borgmann, M. Breitenfeldt, R.B. Cakirli, S. George, F. Herfurth, J.D. Holt, M. Kowalska, S. Kreim, D. Lunney, V. Manea, J. Menéndez, D. Neidherr, M. Rosenbusch, L. Schweikhard, A. Schwenk, J. Simonis, J. Stanja, R.N. Wolf, K. Zuber, Masses of exotic calcium isotopes pin down nuclear forces, *Nature* 498 (7454) (2013) 346–349.
- [25] R.N. Wolf, D. Beck, K. Blaum, C. Böhm, C. Borgmann, M. Breitenfeldt, F. Herfurth, A. Herlert, M. Kowalska, S. Kreim, D. Lunney, S. Naimi, D. Neidherr, M. Rosenbusch, L. Schweikhard, J. Stanja, F. Wienholtz, K. Zuber, On-line separation of short-lived nuclei by a multi-reflection time-of-flight device, *Nucl. Instrum. Methods Phys. Res. A* 686 (2012) 82–90.
- [26] R. Wolf, F. Wienholtz, D. Atanasov, D. Beck, K. Blaum, C. Borgmann, F. Herfurth, M. Kowalska, S. Kreim, Y.A. Litvinov, D. Lunney, V. Manea, D. Neidherr, M. Rosenbusch, L. Schweikhard, J. Stanja, K. Zuber, ISOLTRAP's multi-reflection time-of-flight mass separator/spectrometer, *Int. J. Mass Spectrom.* 349–350 (2013) 123–133, 100 years of Mass Spectrometry.
- [27] T. Dickel, W. Plaß, A. Becker, U. Czok, H. Geissel, E. Haettner, C. Jesch, W. Kinsel, M. Petrick, C. Scheidenberger, A. Simon, M. Yavor, A high-performance multiple-reflection time-of-flight mass spectrometer and isobar separator for the research with exotic nuclei, *Nucl. Instrum. Methods Phys. Res. A* 777 (2015) 172–188.
- [28] M. Reiter, S.A.S. Andrés, J. Bergmann, T. Dickel, J. Dilling, A. Jacobs, A. Kwiatkowski, W. Plaß, C. Scheidenberger, D. Short, C. Will, C. Babcock, E. Dunling, A. Finlay, C. Hornung, C. Jesch, R. Klawitter, B. Kootte, D. Lascar, E. Leistschneider, T. Murböck, S. Paul, M. Yavor, Commissioning and performance of TITAN's Multiple-Reflection Time-of-Flight Mass-Spectrometer and isobar separator, *Nucl. Instrum. Methods Phys. Res. A* 1018 (2021) 165823.
- [29] P. Chauveau, P. Delahaye, G. De France, S. El Abir, J. Lory, Y. Merrer, M. Rosenbusch, L. Schweikhard, R. Wolf, PILGRIM, a multi-reflection time-of-flight mass spectrometer for Spiral2-S3 at GANIL, *Nucl. Instrum. Methods Phys. Res. B* 376 (2016) 211–215, Proceedings of the XVIIth International Conference on Electromagnetic Isotope Separators and Related Topics, EMIS2015, Grand Rapids, MI, U.S.A., 11–15 May 2015.
- [30] B. Liu, M. Brodeur, D. Burdette, J. Kelly, T. Kim, J. Long, P. O'Malley, The performance of the commissioned Notre Dame multi-reflection time-of-flight mass spectrometer, *Nucl. Instrum. Methods Phys. Res. A* 985 (2021) 164679.
- [31] F. Nowacki, A. Obertelli, A. Poves, The neutron-rich edge of the nuclear landscape: Experiment and theory, *Prog. Part. Nucl. Phys.* 120 (2021) 103866.
- [32] M. Hammen, W. Nörtershäuser, D.L. Balabanski, M.L. Bissell, K. Blaum, I. Budinčević, B. Cheal, K.T. Flanagan, N. Frömmgen, G. Georgiev, C. Geppert, M. Kowalska, K. Kreim, A. Krieger, W. Nazarewicz, R. Neugart, G. Neyens, J. Papuga, P.-G. Reinhard, M.M. Rajabali, S. Schmidt, D.T. Yordanov, From calcium to cadmium: Testing the pairing functional through charge radii measurements of $^{100-130}\text{Cd}$, *Phys. Rev. Lett.* 121 (2018) 102501.
- [33] D.T. Yordanov, M.L. Bissell, K. Blaum, M. De Rydt, C. Geppert, M. Kowalska, J. Krämer, K. Kreim, A. Krieger, P. Lievens, T. Neff, R. Neugart, G. Neyens, W. Nörtershäuser, R. Sánchez, P. Vingerhoets, Nuclear charge radii of $^{21-32}\text{Mg}$, *Phys. Rev. Lett.* 108 (2012) 042504.
- [34] R.F. Garcia Ruiz, M.L. Bissell, K. Blaum, A. Ekström, N. Frömmgen, G. Hagen, M. Hammen, K. Hebel, J.D. Holt, G.R. Jansen, M. Kowalska, K. Kreim, W. Nazarewicz, R. Neugart, G. Neyens, W. Nörtershäuser, T. Papenbrock, J. Papuga, A. Schwenk, J. Simonis, K.A. Wendt, D.T. Yordanov, Unexpectedly large charge radii of neutron-rich calcium isotopes, *Nat. Phys.* 12 (6) (2016) 594–598.
- [35] P.-G. Reinhard, W. Nazarewicz, Toward a global description of nuclear charge radii: Exploring the Fayans energy density functional, *Phys. Rev. C* 95 (2017) 064328.
- [36] K. Minamisono, D.M. Rossi, R. Beerwerth, S. Fritzsche, D. Garand, A. Klose, Y. Liu, B. Maaß, P.F. Mantica, A.J. Miller, P. Müller, W. Nazarewicz, W. Nörtershäuser, E. Olsen, M.R. Pearson, P.-G. Reinhard, E.E. Saperstein, C. Sumithrarachchi, S.V. Tolokonnikov, Charge radii of neutron deficient $^{32,33}\text{Fe}$ produced by projectile fragmentation, *Phys. Rev. Lett.* 117 (2016) 252501.
- [37] S. Malbrunot-Ettenauer, S. Kaufmann, S. Bacca, C. Barbieri, J. Billowes, M.L. Bissell, K. Blaum, B. Cheal, T. Duguet, R.F.G. Ruiz, W. Gins, C. Gorges, G. Hagen, H. Heylen, J.D. Holt, G.R. Jansen, A. Kanellakopoulos, M. Kortelainen, T. Miyagi, P. Navrátil, W. Nazarewicz, R. Neugart, G. Neyens, W. Nörtershäuser, S.J. Novario, T. Papenbrock, T. Ratajczyk, P.-G. Reinhard, L.V. Rodríguez, R. Sánchez, S. Sailer, A. Schwenk, J. Simonis, V. Somà, S.R. Stroberg, L. Wehner, C. Wraith, L. Xie, Z.Y. Xu, X.F. Yang, D.T. Yordanov, Nuclear charge radii of the nickel isotopes $^{58-68,70}\text{Ni}$, *Phys. Rev. Lett.* 128 (2022) 022502.
- [38] H. Hergert, A guided tour of ab initio nuclear many-body theory, *Front. Phys.* 8 (2020).
- [39] T. Miyagi, S.R. Stroberg, J.D. Holt, N. Shimizu, Ab initio multishell valence-space Hamiltonians and the island of inversion, *Phys. Rev. C* 102 (2020) 034320.
- [40] S.J. Novario, G. Hagen, G.R. Jansen, T. Papenbrock, Charge radii of exotic neon and magnesium isotopes, *Phys. Rev. C* 102 (2020) 051303.
- [41] G. Hagen, S.J. Novario, Z.H. Sun, T. Papenbrock, G.R. Jansen, J.G. Lietz, T. Duguet, A. Tichai, Angular-momentum projection in coupled-cluster theory: structure of ^{34}Mg , 105, 2022, 064311.
- [42] P. Plattner, The Charge Radius of ^{26m}Al and the Design of an Advanced Optical Detection Region for Collinear Laser Spectroscopy (Ph.D. thesis), University Innsbruck, 2022.
- [43] S. Kaufman, High-resolution laser spectroscopy in fast beams, *Opt. Commun.* 17 (3) (1976) 309–312.
- [44] M. Lange, M. Froese, S. Menk, J. Varju, R. Bastert, K. Blaum, J.R.C. Lopez-Urrutia, F. Fellenberger, M. Grieser, R. von Hahn, O. Heber, K.-U. Kühnel, F. Laux, D.A. Orlov, M.L. Rappaport, R. Repnow, C.D. Schröter, D. Schwalm, A. Shornikov, T. Sieber, Y. Toker, J. Ullrich, A. Wolf, D. Zajfman, A cryogenic electrostatic trap for long-time storage of keV ion beams, *Rev. Sci. Instrum.* 81 (5) (2010) 055105.
- [45] H. Wollnik, M. Przewłoka, Time-of-flight mass spectrometers with multiply reflected ion trajectories, *Int. J. Mass Spectrom. Ion Process.* 96 (3) (1990) 267–274.
- [46] D. Zajfman, O. Heber, L. Vejby-Christensen, I. Ben-Itzhak, M. Rappaport, R. Fishman, M. Dahan, Electrostatic bottle for long-time storage of fast ion beams, *Phys. Rev. A* 55 (1997) R1577–R1580.
- [47] W.H. Benner, A gated electrostatic ion trap to repetitiously measure the charge and m/z of large electrostatic ions, *Anal. Chem.* 69 (20) (1997) 4162–4168.
- [48] C. Kanitz, Construction and Characterization of a Paul Trap for Laser Spectroscopy of Exotic Radionuclides in an MR-ToF Device (M.Sc. thesis), Friedrich-Alexander-University Erlangen-Nürnberg, 2019.
- [49] S. Lechner, Laser Spectroscopy of Antimony Isotopes and the Design of a Cryogenic Paul Trap (Ph.D. thesis), Technical University Vienna, 2021.
- [50] Y. Kudryavtsev, P. Creemers, R. Ferrer, C. Granados, L. Gaffney, M. Huyse, E. Mogilevskiy, S. Raeder, S. Sels, P. Van den Bergh, P. Van Duppen, A. Zadornaya, A new in-gas-laser ionization and spectroscopy laboratory for off-line studies at KU Leuven, *Nucl. Instrum. Methods Phys. Res. B* 376 (2016) 345–352, Proceedings of the XVIIth International Conference on Electromagnetic Isotope Separators and Related Topics, EMIS2015, Grand Rapids, MI, U.S.A., 11–15 May 2015.

- [51] V. Fedosseev, K. Chrysalidis, T. Goodacre, B. Marsh, S. Rothe, C. Seiffert, K. Wendt, Ion beam production and study of radioactive isotopes with the laser ion source at ISOLDE, *J. Phys. G: Nucl. Part. Phys.* 44 (2017) 084006.
- [52] R.N. Wolf, G. Marx, M. Rosenbusch, L. Schweikhard, Static-mirror ion capture and time focusing for electrostatic ion-beam traps and multi-reflection time-of-flight mass analyzers by use of an in-trap potential lift, *Int. J. Mass Spectrom.* 313 (2012) 8–14.
- [53] C. Breitenfeldt, M.W. Froese, K. Blaum, S. George, M. Grieser, M. Lange, S. Menk, R. Repnow, D. Schwalm, L. Schweikhard, R. von Hahn, A. Wolf, Spreading times of ion-bunches in the cryogenic trap for fast ion beams, *Int. J. Mass Spectrom.* 396 (2016) 1–4.
- [54] P. Fischer, S. Knauer, G. Marx, L. Schweikhard, In-depth study of in-trap high-resolution mass separation by transversal ion ejection from a multi-reflection time-of-flight device, *Rev. Sci. Instrum.* 89 (1) (2018) 015114.
- [55] D. Manura, D. Dahl, SIMION 8.1 User Manual, 2008.
- [56] D. Manura, SIMION HS1 collision model REV4, 2007.
- [57] H. Frånberg, P. Delahaye, J. Billowes, K. Blaum, R. Catherall, F. Duval, O. Gianfrancesco, T. Giles, A. Jokinen, M. Lindroos, D. Lunney, E. Mane, I. Podadera, Off-line commissioning of the ISOLDE cooler, *Nucl. Instrum. Methods Phys. Res. B* 266 (19) (2008) 4502–4504, Proceedings of the XVth International Conference on Electromagnetic Isotope Separators and Techniques Related to their Applications.
- [58] S. Schwarz, G. Bollen, R. Ringle, J. Savory, P. Schury, The LEBIT ion cooler and buncher, *Nucl. Instrum. Methods Phys. Res. A* 816 (2016) 131–141.
- [59] B. Barquest, G. Bollen, P. Mantica, K. Minamisono, R. Ringle, S. Schwarz, C. Sumithrarachchi, RFQ beam cooler and buncher for collinear laser spectroscopy of rare isotopes, *Nucl. Instrum. Methods Phys. Res. A* 866 (2017) 18–28.
- [60] I. Podadera, M. Lindroos, R. Catherall, T. Giles, H. Franberg, J. Billowes, F. Duval, E. Mane, P. Delahaye, A. Jokinen, ISCOOL: cooled and bunched beams for ISOLDE, 2007.
- [61] P. Fischer, S. Knauer, G. Marx, L. Schweikhard, Non-isobaric time-of-flight correction for isobar resolving in MR-ToF mass spectrometry, *Int. J. Mass Spectrom.* 432 (2018) 44–51.
- [62] M. Rosenbusch, M. Wada, P. Schury, Y. Ito, H. Ishiyama, S. Ishizawa, Y. Hirayama, S. Kimura, T. Kojima, H. Miyatake, J. Moon, T. Niwase, T. Sonoda, A. Takamine, Y. Watanabe, H. Wollnik, A new multi-reflection time-of-flight mass spectrograph for the SLOWRI facility, *Nucl. Instrum. Methods Phys. Res. B* 463 (2020) 184–188.
- [63] W. Ansbacher, Y. Li, E. Pinnington, Precision lifetime measurement for the 3p levels of Mg II using frequency-doubled laser radiation to excite a fast ion beam, *Phys. Lett. A* 139 (3) (1989) 165–169.
- [64] D.L. Moehring, B.B. Blinov, D.W. Gidley, R.N. Kohn, M.J. Madsen, T.D. Sander-son, R.S. Vallery, C. Monroe, Precision lifetime measurements of a single trapped ion with ultrafast laser pulses, *Phys. Rev. A* 73 (2006) 023413.
- [65] D. Manura, SIMION Simplex optimizer, 2007.
- [66] National Nuclear Data Center, Brookhaven National Laboratory, 2022.
- [67] G.E.P. Box, M.E. Muller, A note on the generation of random normal deviates, *Ann. Math. Stat.* 29 (2) (1958) 610–611.
- [68] F. Wienholtz, K. Blaum, J. Kartheim, D. Lunney, S. Malbrunot-Ettenauer, V. Manea, M. Mougeot, L. Schweikhard, T. Steinsberger, R. Wolf, Improved stability of multi-reflection time-of-flight mass spectrometers through passive and active voltage stabilization, *Nucl. Instrum. Methods Phys. Res. B* 463 (2020) 348–356.
- [69] P. Fischer, L. Schweikhard, Multiple active voltage stabilizations for multi-reflection time-of-flight mass spectrometry, *Rev. Sci. Instrum.* 92 (6) (2021) 063203.
- [70] P. Schury, M. Wada, H. Wollnik, J.-Y. Moon, T. Hashimoto, M. Rosenbusch, High-stability, high-voltage power supplies for use with multi-reflection time-of-flight mass spectrographs, *Rev. Sci. Instrum.* 91 (1) (2020) 014702.
- [71] Analog Devices, LTSpice simulation software, 2007.
- [72] V. Batteiger, S. Knünz, M. Herrmann, G. Saathoff, H.A. Schüssler, B. Bernhardt, T. Wilken, R. Holzwarth, T.W. Hänsch, T. Udem, Precision spectroscopy of the $3s - 3p$ fine-structure doublet in Mg^+ , *Phys. Rev. A* 80 (2009) 022503.
- [73] K. König, K. Minamisono, J. Lantis, S. Pineda, R. Powel, Beam energy determination via collinear laser spectroscopy, *Phys. Rev. A* 103 (2021) 032806.
- [74] C. Gorges, L.V. Rodríguez, D.L. Balabanski, M.L. Bissell, K. Blaum, B. Cheal, R.F. Garcia Ruiz, G. Georgiev, W. Gins, H. Heylen, A. Kanellakopoulos, S. Kaufmann, M. Kowalska, V. Lagaki, S. Lechner, B. Maaß, S. Malbrunot-Ettenauer, W. Nazarewicz, R. Neugart, G. Neyens, W. Nörtershäuser, P.-G. Reinhard, S. Sailer, R. Sánchez, S. Schmidt, L. Wehner, C. Wraith, L. Xie, Z.Y. Xu, X.F. Yang, D.T. Yordanov, Laser spectroscopy of neutron-rich tin isotopes: A discontinuity in charge radii across the $N = 82$ shell closure, *Phys. Rev. Lett.* 122 (2019) 192502.
- [75] H. Heylen, C.S. Devlin, W. Gins, M.L. Bissell, K. Blaum, B. Cheal, L. Filippin, R.F.G. Ruiz, M. Godefroid, C. Gorges, J.D. Holt, A. Kanellakopoulos, S. Kaufmann, Á. Koszorús, K. König, S. Malbrunot-Ettenauer, T. Miyagi, R. Neugart, G. Neyens, W. Nörtershäuser, R. Sánchez, F. Sommer, L.V. Rodríguez, L. Xie, Z.Y. Xu, X.F. Yang, D.T. Yordanov, High-resolution laser spectroscopy of $^{27-32}Al$, *Phys. Rev. C* 103 (2021) 014318.
- [76] S.V. Pineda, K. König, D.M. Rossi, B.A. Brown, A. Incorvati, J. Lantis, K. Minamisono, W. Nörtershäuser, J. Piekarewicz, R. Powel, F. Sommer, Charge radius of neutron-deficient ^{54}Ni and symmetry energy constraints using the difference in mirror pair charge radii, *Phys. Rev. Lett.* 127 (2021) 182503.
- [77] A.J. Miller, K. Minamisono, A. Klose, D. Garand, C. Kujawa, J.D. Lantis, Y. Liu, B. Maaß, P.F. Mantica, W. Nazarewicz, W. Nörtershäuser, S.V. Pineda, P.-G. Reinhard, D.M. Rossi, F. Sommer, C. Sumithrarachchi, A. Teigelhöfer, J. Watkins, Proton superfluidity and charge radii in proton-rich calcium isotopes, *Nat. Phys.* 15 (5) (2019) 432–436.
- [78] W. Nörtershäuser, D. Tiedemann, M. Žáková, Z. Andjelkovic, K. Blaum, M.L. Bissell, R. Cazan, G.W.F. Drake, C. Geppert, M. Kowalska, J. Krämer, A. Krieger, R. Neugart, R. Sánchez, F. Schmidt-Kaler, Z.-C. Yan, D.T. Yordanov, C. Zimmermann, Nuclear charge radii of $^{7,9,10}Be$ and the one-neutron halo nucleus ^{11}Be , *Phys. Rev. Lett.* 102 (2009) 062503.